AD-A150 734 DETERMINATION OF IONOSPHERIC ELECTRON DENSITY PROFILES 1/1
FROM SATELLITE UV (..(U) AIR FORCE GEOPHYSICS LAB
HANSCOM AFB MA D J STRICKLAND ET AL. 17 MAY 84
UNCLASSIFIED AFGL-TR-84-0140 F/G 4/1 NL

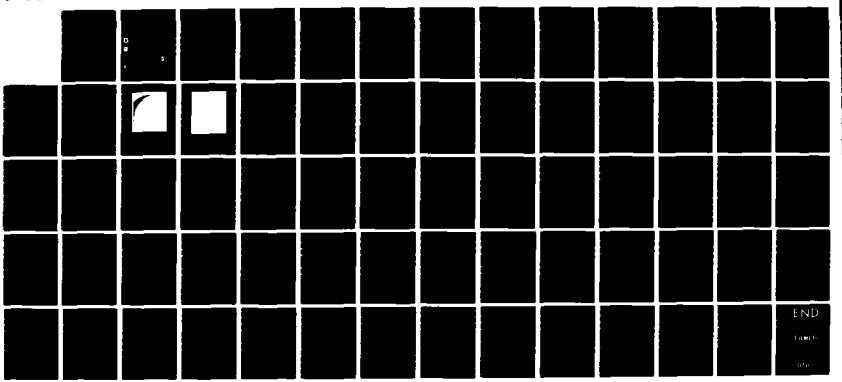

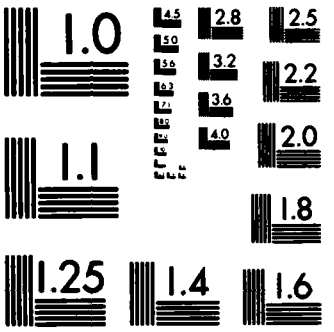

MICROCOPY RESOLUTION TEST CHART
NATIONAL BUREAU OF STANDARDS-1963-A

AFGL-TR-84-0140
ENVIRONMENTAL RESEARCH PAPERS, NO. 880

Determination of Ionospheric Electron Density Profiles From Satellite UV Emission Measurements

D. J. STRICKLAND
R. E. DANIELL, Jr.
D. DECKER
J. R. JASPERSE
H. C. CARLSON

17 May 1984

IONOSPHERIC PHYSICS DIVISION
PROJECT DMSP, 4643
AIR FORCE GEOPHYSICS LABORATORY
HANSCOM AFB, MA 01731

This report has been reviewed by the ESD Public Affairs Office (PA) and is releasable to the National Information Service (NTIS).

"This technical report has been reviewed and is approved for publication."

FOR THE COMMANDER

Herbert C. Carlson, Jr.
Branch Chief

Robert A. Skrivanek, Director
Division Director

Qualified requestors may obtain additional copies from the Defense Technical Information Center. All others should apply to the National Technical Information Service.

If your address has changed, or if you wish to be removed from the mailing list, or if the addressee is no longer employed by your organization, please notify AFGL/DAA, Hanscom AFB, MA 01731. This will assist us in maintaining a current mailing list.

Do not return copies of this report unless contractual obligations or notices on a specific document requires that it be returned.

Unclassified

SECURITY CLASSIFICATION OF THIS PAGE

REPORT DOCUMENTATION PAGE

1a. REPORT SECURITY CLASSIFICATION: Unclassified	1b. RESTRICTIVE MARKINGS: None
2a. SECURITY CLASSIFICATION AUTHORITY: N/A	3. DISTRIBUTION/AVAILABILITY OF REPORT: Approved for public release; distribution unlimited.
2b. DECLASSIFICATION/DOWNGRADING SCHEDULE: N/A	
4. PERFORMING ORGANIZATION REPORT NUMBER(S): AFGL-TR-84-0140 ERP, No. 880	5. MONITORING ORGANIZATION REPORT NUMBER(S)
6a. NAME OF PERFORMING ORGANIZATION: Air Force Geophysics Laboratory; 6b. OFFICE SYMBOL (If applicable): LIS	7a. NAME OF MONITORING ORGANIZATION
6c. ADDRESS (City, State and ZIP Code): Hanscom AFB, Massachusetts 01731	7b. ADDRESS (City, State and ZIP Code)
8a. NAME OF FUNDING/SPONSORING ORGANIZATION: Space Division; 8b. OFFICE SYMBOL (If applicable): SD	9. PROCUREMENT INSTRUMENT IDENTIFICATION NUMBER: SD/AFGL 84-088
8c. ADDRESS (City, State and ZIP Code): P.O. Box 92960, Worldway Postal Center, Los Angeles, CA 90009	10. SOURCE OF FUNDING NOS.

PROGRAM ELEMENT NO.	PROJECT NO.	TASK NO.	WORK UNIT NO.
35160F	DMSP	04	00
62101F	4643	07	01

11. TITLE (Include Security Classification) Determination of Ionospheric Electron Density Profiles From Satellite UV Emission Measurements

12. PERSONAL AUTHOR(S): D.J. Strickland*; R.E. Daniell, Jr.*, D. Decker**; J.R. Jasperse; H.C. Carlson

13a. TYPE OF REPORT	13b. TIME COVERED	14. DATE OF REPORT (Yr., Mo., Day)	15. PAGE COUNT
Summary	FROM Feb 83 TO Feb 84	1984 May 17	69

16. SUPPLEMENTARY NOTATION
*Beers Associates, Inc., P.O. Box 2549, Reston, VA 22090
**Boston College, Chestnut Hill, MA

17. COSATI CODES		
FIELD	GROUP	SUB. GR.
0401	20	09

18. SUBJECT TERMS (Continue on reverse if necessary and identify by block number)
Global electron density, Electron spectra hardness, Electron density profile, Satellite measurements, UV spectra, UV sensor, (Contd)

19. ABSTRACT (Continue on reverse if necessary and identify by block number)

The possible use of satellite ultraviolet measurements to deduce the ionospheric electron density profile (EDP) on a global basis is discussed. A system concept is considered and analyzed which (a) develops and installs a UV sensor on the DMSP satellite and develops an associated automatic data processing (software) system, (b) utilizes optical data together with DMSP electron density and temperature data to deduce the near real-time EDP near the satellite orbital plane, and (c) transmits this EDP data to be used together with ground-based ionosonde data and GPS total electron content data to specify the global EDP for systems users. The ionosonde and total electron content data would increase the EDP data base generated by the UV data and refine the UV based EDP where coincident data existed.

This report considers (a) the daytime low to midlatitude ionosphere from 90 to 1000 km, (b) the nighttime midlatitude ionosphere from about 250 km to 1000 km, and (c) the auroral E layer from 90 to about 200 km for undisturbed conditions. (Contd)

20. DISTRIBUTION/AVAILABILITY OF ABSTRACT	21. ABSTRACT SECURITY CLASSIFICATION
UNCLASSIFIED/UNLIMITED ☒ SAME AS RPT. ☐ DTIC USERS ☐	Unclassified

22a. NAME OF RESPONSIBLE INDIVIDUAL	22b. TELEPHONE NUMBER (Include Area Code)	22c. OFFICE SYMBOL
John R. Jasperse	(617) 861-3137	AFGL/LIS

DD FORM 1473, 83 APR EDITION OF 1 JAN 73 IS OBSOLETE

SECURITY CLASSIFICATION OF THIS PAGE

18. (Contd)

Ionosonde data
Electron flux.
Optical emission
Total electron content.
Auroral E-spectra
Lyman-Birge-Hopfield (LBH) bands,
Solar flux.
Neutral density
Photon counter
HF communication systems
SPACETRACK radar systems,
OTH systems,
Photoelectron flux,
Precipitating electron spectra,
Spectrometer,
Photometer

19. (Contd)

The spatial resolution for the daytime and nighttime EDP is at least one vertical profile for each square 500 km on a side and for the auroral E layer at least one vertical profile for each square 50 km on a side. Other ionospheric regions were not considered because of frequent occurrence of irregularities or highly variable transport conditions.

In the daytime low to midlatitude ionosphere, no useful optical emissions are available which give a signal directly dependent upon the electron density profile. An indirect method is therefore proposed where the emission feature at 1356 A and at least one of the Lyman-Birge-Hopfield (LBH) bands are used to deduce the O to N_2 density ratio and the absolute scale of the solar flux. This information together with a neutral wind model and time dependent ion continuity equations can be used to determine the EDP. This utilization of deduced parameters (O to N_2 density ratio and scaling factor for solar flux) significantly improves the accuracy of the EDP over a result based on empirical values for these parameters. In the nighttime midlatitude ionosphere, the atomic lines at 1356 A and 6300 A relate sensitively to the electron content near the peak of the EDP and the altitude of the bottomside EDP. Utilizing a time dependent transport approach and an empirical model for the shape of the F layer, F layer profiles from 250 to 1000 km may be obtained. In the auroral E layer, emission features at 1356 A and one or more of the LBH bands may be used to give an indirect determination of the hardness and energy flux of the incident auroral electrons which produce the E layer. Use of this incident electron information in an electron transport/chemistry model yields the EDP from 90 to about 200 km.

Contents

Contents

Illustrations

Tables

Determination of Ionospheric Electron Density Profiles From Satellite UV Emission Measurements

1. EXECUTIVE SUMMARY

1.1 The System Concept

In this report we discuss the possible use of satellite ultraviolet (UV) measurements to deduce the ionospheric electron density profile (EDP) on a global basis. The system concept is: (a) to develop and install a UV sensor on the DMSP satellite and to develop an associated automatic data processing (software) system, (b) to use the optical data together with DMSP electron density and temperature data to deduce the near real-time EDP near the satellite orbital plane, and (c) to transmit this EDP data to be used together with ground-based ionosonde data and GPS total electron content (TEC) data to specify the global EDP for system users. The ionosonde and TEC data would serve two purposes: increase the EDP data base generated by the UV data, and refine the UV based EDP where coincidence data exist.

1.2 The Ionospheric Subregions

In this report we consider the following ionospheric subregions: (a) the daytime low- to mid-latitude ionosphere from 90 to 1000 km, (b) the nighttime midlatitude ionosphere from about 250 to 1000 km, and (c) the auroral E layer from 90 to

(Received for publication 17 April 1984)

about 200 km for undisturbed conditions. The spatial resolution considered for the daytime and nighttime EDP is at least one vertical profile for each square 500 km on a side and for the auroral E layer at least one vertical profile for each square 50 km on a side. The ionospheric subregions excluded from consideration either because of the high frequency of occurrence of irregularities or highly variable transport conditions are the polar caps, the cusp, the auroral F region, and the equatorial nighttime region.

1.3 Use of UV Measurements

(a) In the daytime low- to mid-latitude ionosphere no useful optical emission features have been identified which when measured from the DMSP altitude (~840 km) give a signal directly dependent upon the electron density profile. In this region, we therefore, propose an indirect method where we measure the emission feature at 1356 A and at least one of the Lyman-Birge-Hopfield (LBH) bands to deduce the O to N_2 density ratio and the absolute scale of the solar flux. This information together with a neutral wind model is used to calculate the EDP from first principles using time dependent ion continuity equations. Basing the specified EDP on the above deduced key parameters (O to N_2 density ratio and scaling factor for the solar flux) significantly improves the accuracy of the EDP over a result based on empirical values of these parameters.

(b) In the nighttime midlatitude ionosphere there are at least two useable emission features which give a signal directly dependent on the EDP; they are the atomic lines at 1356 A and 6300 A. These respectively relate sensitively to the electron content near the peak of the EDP and the altitude of the bottomside EDP. To extract the most accurate EDP from these observations, we are currently investigating two approaches: (1) a time dependent transport approach where the neutral winds and possibly the electric field are deduced from the optical emission measurements, and (2) an empirical model where the shape of the F layer is fixed and its location in altitude and its absolute value are determined by the emission features. This would produce F layer profiles from about 250 to 1000 km.

(c) In the auroral E layer, in the absence of arcs, we can use the emission features at 1356 A and one or more of the LBH bands to give an indirect determination of the hardness and energy flux of the incident auroral electrons which produce the E layer. The EDP is then determined from 90 to about 200 km using this incident electron information in our electron transport/chemistry model.

1.4 Present Uncertainties and Planned Model EDP Improvements

We find the proposed observables favorable in large part because of the large fraction of the required 60-1000 km global coverage they can provide (see Table 1)

including the bonus of sensing a broad area (rather than a single line) under the sub-orbital track. The feasibility of the given approach rests upon our own recent advances in state-of-the-art capabilities simultaneously pressed into parallel areas: hardware development of UV sensors capable of measuring complete global day and nighttime emissions, and physical modeling of ionospheric processes strongly coupled to selected optical emissions. The hardware development has demonstrated success on both a shuttle and a satellite recently flown; the software development has been successfully tested against field experimental data.

Table 1. Available Sensor Options

Subregions	UV	Topside Sounder	X-Ray
Daytime Low- to Mid-Latitude			
Bottomside	Yes	No	No
Topside	Yes	Yes	No
Nighttime Low- to Mid-Latitude			
Bottomside	Yes	No	No
Topside	Yes	Yes	No
Auroral			
E I	Yes	No	Yes
D Layer	No	No	Yes

Very few data exist for quantitative determination of error bars for this EDP system concept due to scarcity of coincident optical and EDP measurements. This will be a subject of study in FY84 and 85. In the meantime, the expected EDP improvement must be discussed more in relative than absolute terms. Meaningful statements, however, can still be made.

Errors in our ab-initio daytime model are comparable to those of the other state-of-the-art models for known conditions (order ± 30%). The factors of prime importance, as noted in Section 1.3, are the solar EUV flux, the O/N_2 density ratio, and the neutral wind. Errors in excess of a factor of 2 can be expected in the calculated EDP without direct knowledge of these factors. Optical observations will provide the needed knowledge for the first two factors and should lead to acceptable accuracy in the E and lower F regions. Near and above the peak of the EDP, transport effects are important. Means for minimizing uncertainties in the calculated EDP due to errors inherent in models for the transport term are being studied in FY84 and 85. Possible thermal and light ion composition effects on the

topside EDP will also be studied in FY 84 and 85. Overall errors should furthermore be significantly reduced with the aid of ionosonde and TEC data cited above. Such data allow spot checking of the UV deduced EDP through which adjustments can be made if necessary due to such factors as optical sensor degradation.

Errors in deduced nighttime n_e profiles arise from variable transport and uncertainties in temperature and light ion composition. The major effects of variable transport are changes in the overall magnitude of the EDP and location of the EDP maximum. A less important effect is a change in the EDP shape. The proposed observables directly specify both the electron concentration near the peak and the height of the peak, thus eliminating most of the uncertainty caused by the above major changes. The more minor change (that of shape) remains a source of EDP error for this approach, perhaps being a couple of tens of percent at times of strong transport. Means of correcting for this will be studied in FY84 and 85. Topside effects due to temperature and light ion composition will be significant, and in FY84 and 85 we will identify the optimum approach to merging the EDP determined near and below the peak by optical emissions to the boundary conditions near 800 km given by DMSP in situ sensors.

In the auroral E layer, for arc-free conditions, the EDP from 90 to 200 km should be achievable to within ± 40% by the method proposed in this report. Techniques to reduce this error will be studied in FY85.

2. BACKGROUND

2.1 Objective

The objective of this work is to determine the feasibility of deducing the EDP on a global basis in near real time from remote, passive optical and other measurements made from a satellite platform. It is also our objective to develop specific computer codes (software) to convert the satellite measurements to electron density profiles. In this report we discuss the results of these studies through the end of FY83.

2.2 Early Work

Air Weather Service has expressed its requirement for global electron density profiles with MAC SON 02-80. This approved statement of operational need is the driving force behind the effort to equip a future DMSP satellite with instrumentation to measure electron densities. Unfortunately, this measurement from space is not straightforward and AFGL embarked on a research program to develop the theory, the models, and the sensors to achieve the DMSP goals.

AFGL's approach was to formulate a first principles ionospheric model within the 6.1 program and develop and build a UV ionospheric mapper within the 6.2 program. By the end of 1981, the ionospheric modeling had progressed to the point where it appeared feasible to relate electron density profiles to UV optical emissions. The DMSP SPO was interested and provided AFGL with funding in FY82 and 83 to perform some additional, system specific, feasibility studies and computer code development.

The development of the UV instrumentation also made considerable progress and when DNA decided to fly the HILAT satellite, AFGL took advantage of that opportunity to test the UV Ionospheric Mapper. For the HILAT satellite, the mission objectives tended to focus on auroral zone events, but the mid- and low-latitude requirements of DMSP and AWS were also satisfied by this instrument. In fact, even the actual instrument configuration was designed with DMSP satellite dimensions as guidelines.

At AFGL, we have been involved in ionospheric modeling and UV technology for the past fifteen years. The AFGL personnel involved in this specific DMSP effort are Drs. J.R. Jasperse, H.C. Carlson, J.A. Whalen, D.N. Anderson, R.A. Huffman, and R.A. Van Tassel. In addition, several contractors have been working closely with AFGL; they are Drs. D.J. Strickland and R.E. Daniell, Jr. of Beers Associates, Inc., D. Decker of Boston College, C. Meng of Johns Hopkins Applied Physics Laboratory, R. Vondrak of Lockheed, and R. Robinson of Stanford Research International.

2.3 System Concept

The development of a sensor-software system requires the successful completion of a number of steps. They are:

(1) Performance of feasibility studies and the development of computer codes for determining the EDP from remote passive optical and other measurements.
(2) Installation of a UV sensor on DMSP to scan several ionospheric emission features in the near nadir direction.
(3) Utilization of these data together with other data (electron temperature and possibly electron density at the DMSP altitude from other DMSP sensors) to determine the EDP from 90 to 1000 km near the satellite track.

(4) Utilization of the DMSP EDP data with other data as an input to a large scale model to determine the global EDP in near-real time. Other useful data would be the ground-based ionosonde network providing bottomside EDP measurements and the GPS system providing TEC measurements. These additional data could provide an accurate calibration of the UV sensor whenever the DMSP passed near the region being sampled by these systems.

(5) Communicate the products of the global EDP model (bottomside profiles, topside profiles, TEC, foF2, and so on) to system users. Systems in need of this information would include HF communications systems, OTH systems, SPACETRACK radar systems, and classified systems.

The system concept is illustrated in Figure 1 where we show the DMSP and GPS satellites sensing the EDP with OTH and SPACETRACK radar systems utilizing the results.

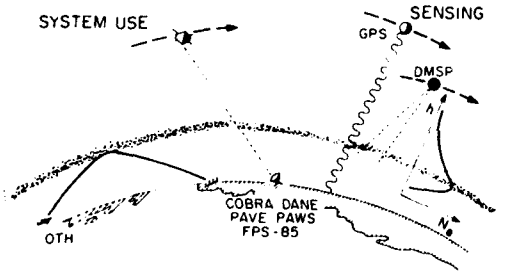

Figure 1. Global Electron Density Sensing and System Use

2.4 Ionospheric Subregions

The ionosphere is generally divided into four altitude regions designated D, E, F_1, and F_2 in order of increasing altitude. Three latitude regions—high, middle, and low—are also recognized. At night the poleward boundary of the mid-latitude region is defined by the midlatitude trough discovered by Muldrew[1] using Alouette I topside sounder data. For our purposes here we identify the boundary between the low and middle latitude regions as the latitude below which the significant equatorial EDP enhancements occur by day (Appleton Anomaly), and significant irregularities characteristic of the equatorial region (such as equatorial

1. Muldrew, D. B. (1965) F-layer ionization troughs deduced from Alouette data, J. Geophys. Res. 70:2635.

spread F) are found at night (generally within 20° of the geomagnetic equator; Fejer and Kelley[2]). Here we take the 20° geomagnetic latitude contour as the nominal equatorward boundary for the midlatitude ionosphere.

The system concept described in Section 2.3 is expected to be feasible, with significantly improved accuracy as discussed in Section 1, in the following three ionospheric subregions: (1) the daytime low- to mid-latitude region from 90 to 1000 km; (2) the nighttime mid-latitude region from about 200 to 1000 km; and (3) the auroral E-layer from 90 to about 200 km for undisturbed conditions. In Sections 3 through 5, we discuss each subregion in some detail. Note that sporadic E has been excluded from consideration.

In Figures 2 and 3, we show two satellite images of the terrestrial ionosphere as seen from space in the UV. Figure 2 is from an instrument on the Dynamics Explorer (DE) satellite having a low spectral and areal resolution. It shows the sunlit side of the Earth, the day-night terminator, and the entire nighttime auroral oval. Note that even this state-of-the-art instrument is not sufficiently sensitive to sense the faint sub-auroral nighttime UV. In Figure 3 we show an image of the daytime high-latitude ionosphere near Hudson's Bay from the AFGL UV sensor on the HILAT satellite. The emission feature shown is OI 1356 A with a spatial resolution higher than that of Figure 2. AFGL instrumentation of this type will be capable of and is planned for obtaining daytime and nighttime EDP's.

3. DAYTIME MIDLATITUDE IONOSPHERE

In this section we discuss the issues and our recent work in specifying the EPD from 90 to 1000 km using UV sensing. Our goal is to convert nadir viewing intensities of key optical features such as OI 1356 A and LBH bands into an EDP in real time. This will require either an empirical model or a data base developed from first principles modeling now in progress. The key parameters in such a model or data base are:

(1) the solar extreme UV (EUV) energy,
(2) the N_2, O_2, and O densities,
(3) the neutral wind and electric field, and
(4) temperatures (T_e, T_i, and T_n).

---

2. Fejer, B.G., and Kelley, M.C. (1980) Ionospheric irregularities, Rev. Geophys. Space Phys. 18:401.

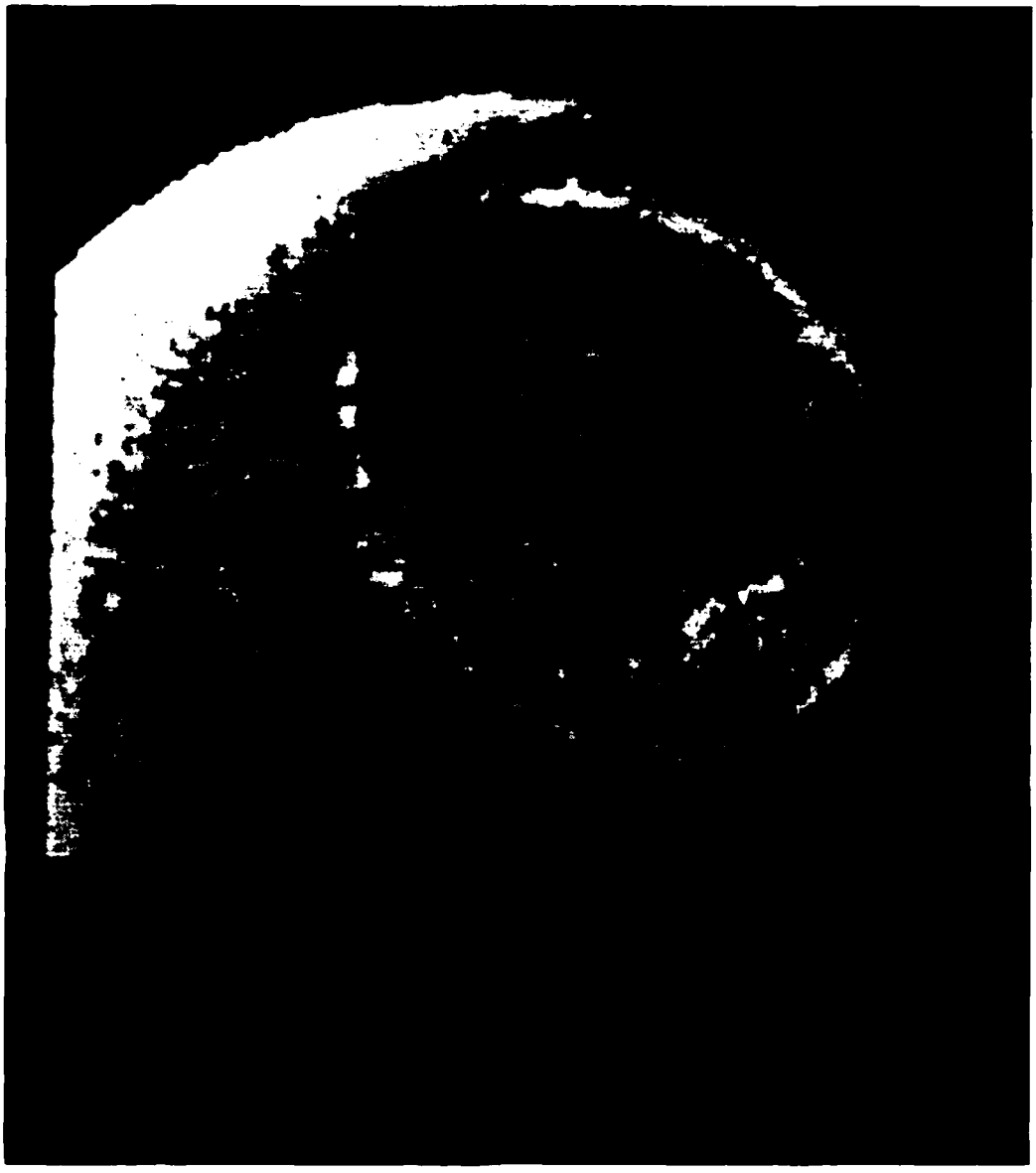

Figure 2. UV Image From DE Satellite

Their importance in terms of present day uncertainties depends on altitude. Items (1) and (2) dominate in the E region and lower F region ($\lesssim$220 km; regime 1) while all four items are important at higher altitudes (regime 2).

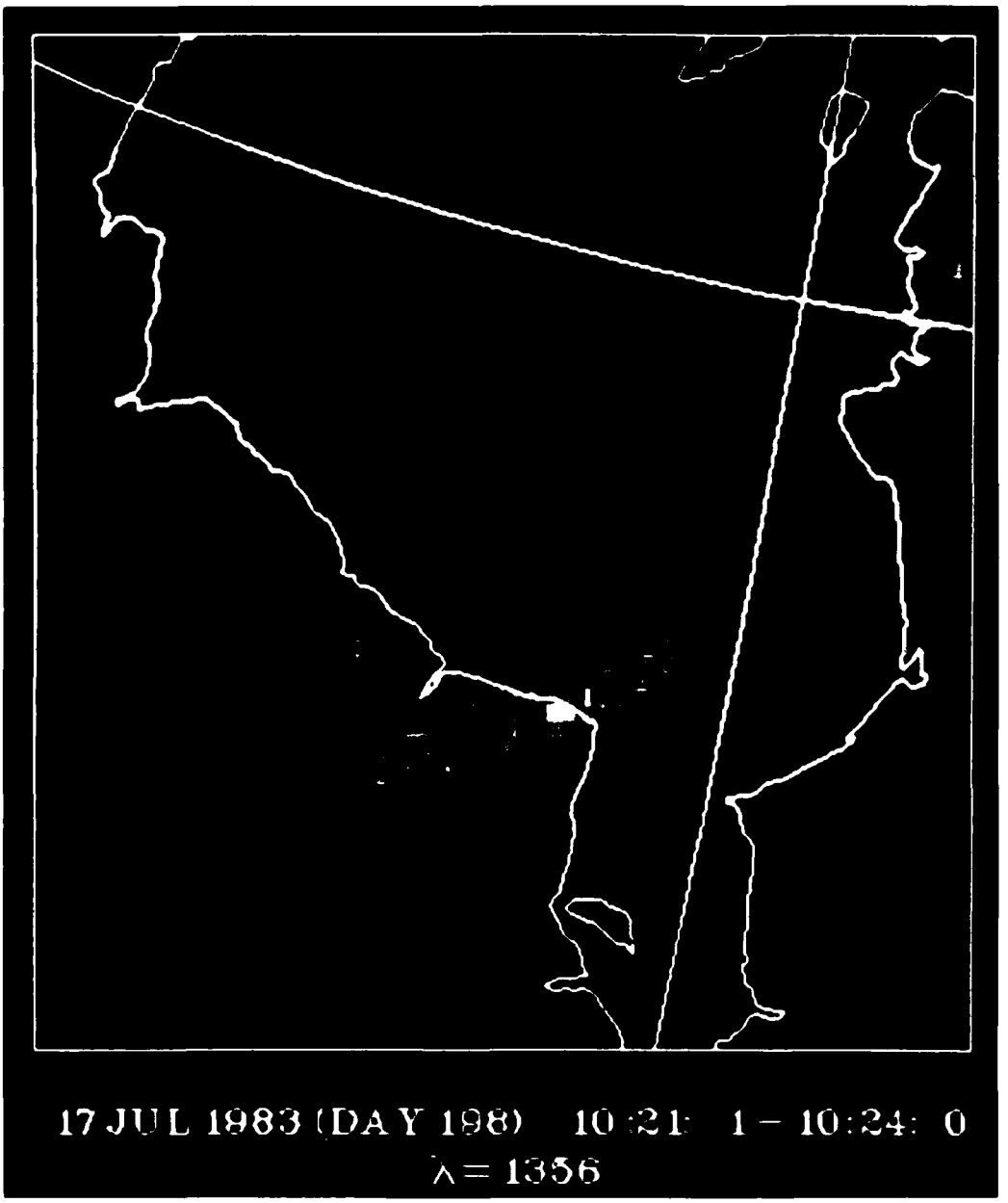

Figure 3. UV Image From the HILAT Satellite

We face two basic issues. They are:

(1) "How well can the EDP be determined knowing the above parameters?" and

(2) "How well can these parameters be known at any given time and location?".

Investigations by us and by Meier and colleagues at NRL[3,4,5] have demonstrated that observations of intensities at selected wavelengths from the near UV (NUV) to the EUV will determine items (1) and (2). Accuracy still remains an issue to which ongoing effort is being directed. In particular, observations of N_2 LBH bands and OI 1356 A provide a good measure of the incoming rate of solar energy responsible for maintaining the daytime ionosphere. They also determine the O density profile relative to that for N_2. This is important since the O/N_2 ratio is known to vary significantly with time and location and to be a major factor controlling both the efficiency with which solar radiation produces long-lived O^+ ions, as well as the EDP loss rate.

There is little hope that optical emissions can be used to determine changes in the shape of the solar EUV spectrum. This is not a serious problem since actual changes do not have a major effect on the shape of altitude profiles of excitation rates producing optical emissions and ionization rates producing n_e. The key parameter with regard to the solar source is energy content which optical emissions will nicely provide. Changes in spectral shape can be accounted for by interpolating on observed spectra obtained for a range of solar activities. The interpolation variable is $F_{10.7}$, the 10.7 cm solar flux. Our plans are to model the changes using rocket solar data such as those obtained by AFGL.[6,7,8]

3.1 Typical Electron and Ion Profiles and UV Emissions

This section presents three figures of representative conditions. Figure 4 is an example of the density profiles from 90 to 1000 km for the major constituents of the daytime midlatitude ionosphere. Figures 5 and 6 are examples of daytime midlatitude airglow spectra.

The number densities given in Figure 4 are typical for daytime midlatitude conditions.[9] The ion densities are from Johnson[10] based on rocket measurements below 240 km and satellite measurements above 400 km. The neutral densities are from the model of Jacchia[11] for an exospheric temperature of 1000 K.

(Due to the large number of references cited above, they will not be listed here. See References, page 51.)

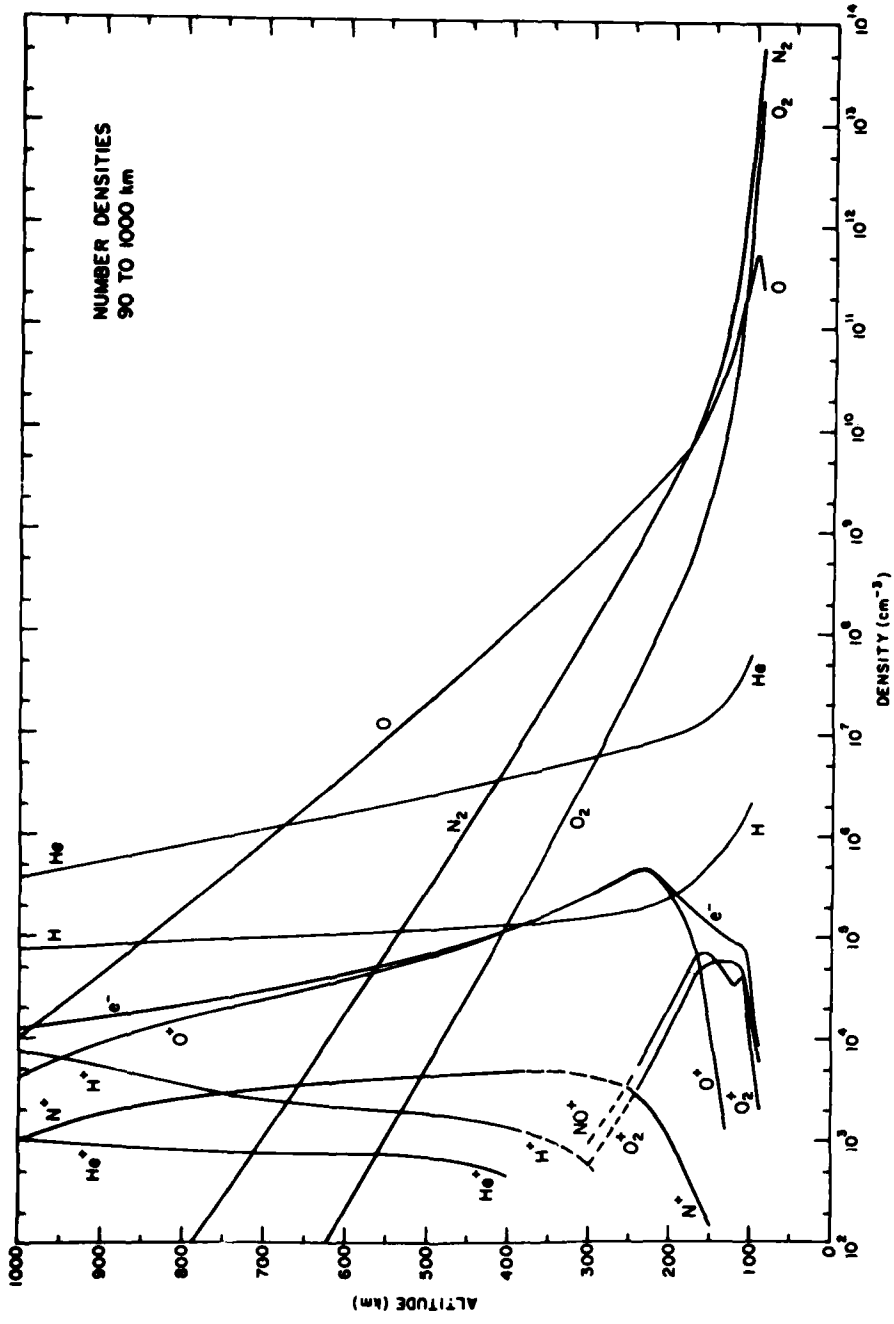

Figure 4. Number Densities From 90 to 100 km. The ion densities are from Johnson[10] and are rocket measurements below 240 km and satellite measurements above 400 km. The neutral densities are from the model of Jacchia[11] for an exospheric temperature of 1000 K. These are close to the values used by Johnson. The solar intensity at 10.7 cm was about 80 when the ion densities were measured. These data are for midlatitude conditions

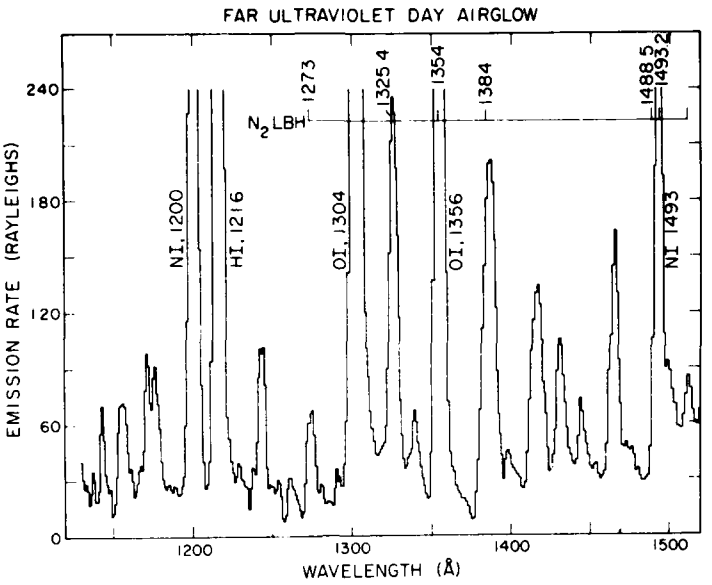

Figure 5. Average of Six-Pulse Counting Spectra With a Horizontal Aspect Showing Enhancements in the Optically Thin Emissions. (Spectrum has been smoothed by sliding averages of adjacent bins and the error bars reflect one standard deviation in low-level signals near 1260 A (from Takacs and Feldman[12])

In particular we can see the basic features of the electron density profile. There is maximum density (F_2 peak) between 200 km to 300 km, a decrease in density above the F_2 peak (the topside), a decrease in density below the F_2 peak (bottomside), and a small peak or ledge in the E region.

Figure 5 from Takacs and Feldman[12] shows the type of airglow spectrum in the far UV (FUV) that can be detected in the daytime midlatitude ionosphere. These particular data come from a December 11, 1972 rocket experiment flown from the White Sands Missile Range. Prominent features include LBH bands, OI 1304 A, OI 1356 A, and NI 1493 A.

12. Takacs, P. Z., and Feldman, P. D. (1977) Far ultraviolet atomic and molecular nitrogen emissions in the dayglow, J. Geophys. Res. 82:5011.

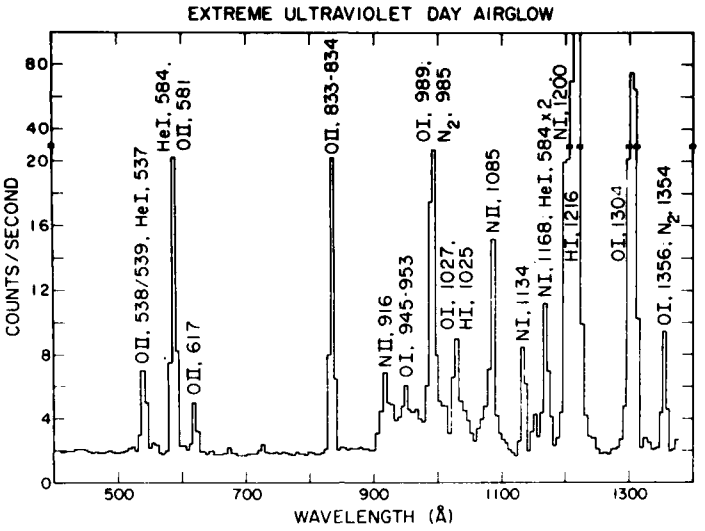

Figure 6. EUV Dayglow Spectrum at 600-km Altitude. Spectrum was obtained by averaging individual spectra taken while the spacecraft was between 50° N and 50° S, in the noon-midnight meridian in the period March 5-15, 1979, with the instrument pointed near nadir (zenith angle between 120° and 150°). The solid line labeled 100 R indicates instrument sensitivity in 100 R per wavelength bin. Representative 1 σ error bar is shown on the lower right-hand side of the diagram (from Chakrabarti et al[13])

Figure 6, taken from Chakrabarti et al[13] shows an airglow spectrum in the EUV for daytime midlatitude conditions as viewed by a satellite instrument looking in the nadir direction. These particular data are from the U.S. Air Force STP 78-1 satellite at 600 km. Table 2 gives a list of prominent emission features in Figures 5 and 6 under investigation by us.

3.2 Approach

Our approach to determining the EDP is to develop a physical model which can then be parameterized and readily scaled by those physical observables which most directly and sensitively determine the EDP. We have identified optical observables that both satisfy these scaling requirements and are measurable to the necessary accuracy using current technology.

13. Chakrabarti, S., Parasce, F., Bowyer, S., Kimble, R., and Kumar, S. (1983) The extreme ultraviolet day airglow, J. Geophys. Res. 88:4898.

Table 2. Selected FUV and EUV Features Under Investigation

Feature	σ_{O_2} (10^{-18} cm^2)	Reference	Opt. Thick
NI 1493	11	a	No
LBH 1493	11	a	No
LBH 1464	12	a	No
LBH {1416, 1412}	12	a	No
LBH {1384, 1382}	13	a	No
LBH 1354	7.1	a	No
LBH 1325	2.0	a	No
LBH 1273	0.09	a	No
OI 1356	7.3	a	No
OI 1304	0.5	a	Yes
NI 1200	1.0	b	Yes
NI 1168	0.02	b	No
NI 1134	0.8	b	No
NII 1085	2.0	b	No
{OI 1027, HI 1026}	1.0	b	Yes
OI 989	2.6	c	Yes
NI 953	3.5	c	No
NII 916	6.7	c	No

a. Watanabe, K. M., Zelifoff, M., and Inn, E. C. Y. (1953) Absorption coefficients of oxygen in the vacuum ultraviolet J. Chem. Phys. 21:1026.

b. Watanabe, K. (1958) Ultraviolet absorption processes in the upper atmosphere, Advan. Geophys. 5:153.

c. Matsunaga, F. M., and Watanabe, K. (1967) Total and photoionization coefficients and dissociation of O_2 in the 580-1070 A region, Sci. Light 16:31.

We use a first principles approach in the physical model employed to determine the EDP. The method of Jasperse[14, 15] is applied in the E and lower F regions. The method of Anderson[16] is applied to the upper F region. Together these approaches require the four parameters discussed at the beginning of Section 3. As noted there, downward viewing intensities of features such as OI 1356 A and LBH bands are functions of parameters 1 and 2 (solar EUV energy flux and the neutral densities). The code of Jasperse provides these functional relationships and thus enables the given parameters to be specified from the optical data.

The photoelectron distribution function F(E, z) (e/cm^2-s-eV-4π sr) is the first quantitity calculated by the above code. The needed volume production rates are then obtained from

$$P_i(z) = n(z) \int_{E_i}^{E_{max}} F(E, z)\, \sigma\,(E)\, dE$$

where P_i refers to either emission or ionization. The density n(z) refers to the impacting species and σ is the corresponding cross section (cm^2). Integration over z with proper accounting of pure photon absorption gives the intensity where P_i is an emission rate. This intensity accounts for nearly all emission since P_i is dominant in the E and lower F regions.

The EDP is given by the sum of the calculated ion densities. These come from the continuity equations

$$\frac{\partial n_i}{\partial t} + \nabla \cdot n_i \bar{v}_i = P_i - L_i$$

where P_i is the i^{th} ion production rate as defined above, L_i is the loss rate, and $\bar{v}_i$ is the ion transport velocity. In the Jasperse code, these equations are simplified to $P_i - L_i = 0$ for the species treated (O^+, N_2^+, O_2^+, NO^+). This is valid since n_i changes slowly with time and transport produces a minor effect on n_i.

---

14. Jasperse, J. R. (1976) Boltzmann-Fokker-Planck model for the electron distribution function in the earth's ionosphere, Planet. Space Sci. 24:33.

15. Jasperse, J. R. (1977) Electron distribution function and ion concentrations in the earth's lower ionosphere from Boltzmann-Fokker-Planck theory, Planet. Space. Sci. 25:743.

16. Anderson, D. N. (1973) A theoretical study of the ionospheric F region. equatorial anamoly, 1, Theory, Planet. Space. Sci. 21:409.

Near and above the EDP peak, the full continuity equation, as given above, is solved. The dominant species is O^+ throughout most of this region. The Anderson code, as presently used, solves the full equation for the density of O^+ treating in detail diffusion and the effects of the neutral wind. The Jasperse and Anderson codes are run concurrently with matching conditions at their common boundary. The result is a calculated EDP from 100 to 1000 km.

In FY84-85 we will concentrate on optimizing treatment of the transport term. In the present codes, the neutral wind and electric fields used to provide the transport term are, as for any ab-initio model, representative of typical conditions, and are not matched to the specific moment and place of an observation. Having used observations to transcend the limitations of conventional model treatments of production and loss, we will next turn attention to this transport term as the next most serious limitation on the EDP accuracy. We will also address the effects of temperature and light ion composition on the EDP. These effects, quite modest (a few percent) at the peak of the EDP can become significant at higher altitudes. In fact, light ions are known to be the dominant ion above 600 km over much of the dark globe at sunspot minimum. Temperature variations easily produce many tens of percent variations in the EDP at 1000 km day and night. In the present code, the electron and ion temperature profiles are analytic expressions from Strobel and McElroy[17] based on data of Evans[18] and represent typical conditions.

3.3 Comparison Between Theory and Experiment

There exist no data under controlled experimental conditions for testing the proposed scheme against a full observed EDP. We thus discuss four data sets which partially approach the degree of parametric control that would be available from coincident VUV data. Two sets have been completely analyzed; the other two are in progress for FY 84.

(1) Case One: White Sands Missile Range, 23 August 1972.[6]

This case involves rocket data for the solar EUV flux coincident with ground based ionosonde data. This represents a partial control on the production rate and should lead to good bottomside EDP agreement. In Figure 7 we show a plot of the bottomside electron density profile from the ionosonde measurement and a graph of our hybrid calculation for the electron density profile. It should be noted that the estimated errors for the ionosonde measurement were ± 30 km near 120 km and

17. Strobel, D. F., and McElroy, M. B. (1970) The F2-layer at middle latitudes, Planet. Space Sci. 18:1181.

18. Evans, J. V. (1976) The dynamics of the ionosphere and upper atmosphere, in Physics of Solar Planetary Environments, D. J. Williams, Ed., American Geophysical Union, Washington, 630

± 5 km elsewhere. For this case a Jacchia[11] neutral atmosphere with the appropriate parameters for the given day was used in the calculation in addition to the measured solar flux EUV flux. Typical daytime models were used for the electron temperature and neutral winds. With observational control on the solar flux one would expect good EDP agreement in and below the F_1 layer. The agreement in the F_1 layer is in fact respectably within 15%, while the agreement in the E region is within the error bars on the ionosonde EDP. Unfortunately, the unusually large error bar on the ionosonde measurement near 120 km renders the E region agreement of limited quantitative significance. The 25 km or 30% difference in the F_2 peak of the EDP is consistent with any other state-of-the-art ab-initio model calculation, and merely reinforces our intent to pursue the study of the transport term which is in all likelihood the source of this difference.

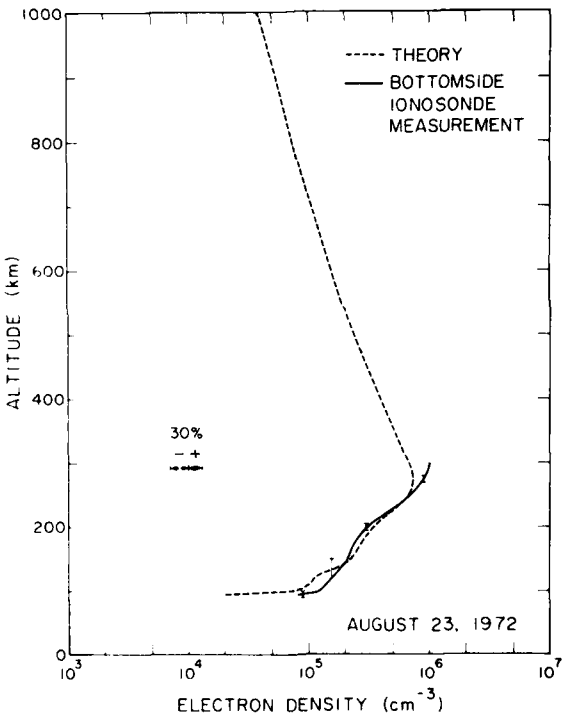

Figure 7. Daytime EDP's on 23 August 1979 Above White Sands Missile Range. A ground based ionosonde provided the measured profile. Rocket solar EUV data were used to obtain the calculated profile

(2) Case Two: ISIS 2 topside sounder, 23 May 1972.

The data considered here come from an ISIS 2 pass at 8:28 UT at 60° north latitude and 38° east longitude. The data were taken from iso-density contours in a sample collection of ISIS 2 observations.[19] Due to reported difficulties in interpretation of sounder data, we have shown the data with ± 50 km error bars. Figure 8 shows two theoretical curves with the topside sounder data. The solid curve shows the calculated profile using our best a priori estimates for the input quantities. We can see that the ab-initio calculated profile is 60% lower than the data but agrees in shape. The dotted curve is a scaled version of the calculated profile fitted to the data. Had this been a nighttime case, we would expect direct UV emissions as discussed in the next section to provide a good estimate of the peak of the EDP, to which the calculated topside EDP shape would then be scaled. This would lead to quite satisfactory agreement for this case. For the daytime case, the dashed curve would be essentially duplicated above 350 km by use of a stronger equatorward wind in the model (as might follow at these latitudes from a high latitude heating event). The excellent agreement of the shape of the model and observed EDP satisfies necessary conditions for the merit of this EDP scheme. However, some additional observable must be added to scale the ab-initio calculated EDP before we can look for the good agreement shown by the dashed curve.

(3) Case Three: HILAT Satellite, July 1983.

The proposed UV sensor was recently flown by AFGL and DNA on a satellite and operated in a mode allowing scaling of calculated EDP to 1356 A observations during overflights of simultaneously operating ionosondes. These data are now being analyzed as part of our FY 84 program.

(4) Case Four: Composite data collection.

We have noted that no data have been identified for which simultaneous measurements of the following have been made: solar EUV spectrum, EDP, ion density profiles, and intensities of features such as OI 1356 A and LBH bands. In the absence of this, we are searching for coincident data within the parameter group obtained from different observing platforms. There are the solar EUV data recorded onboard the AE-E satellite (Hinteregger et al[20]). The operations of the STP 78-1 and S3-4 satellites overlapped that of AE-E. These satellites respectively

---

19. Klumpar, D.M., Ed. (1980) Coordinated Ionospheric and Magnetospheric Observations from the ISIS 2 Satellite by the ISIS 2 Experimeters, 3, (NSSDC/WDC-A-R+S, 80).

20. Hinteregger, H.E., Bedo, D.E., and Manson, J.E. (1973) The EUV spectral photometer on atmospheric explorer, Radio Sci. 8:349.

carried EUV[21] and FUV spectrometers.[22] There were also rocket experiments during the operation of AE-E. One has been reported by Gentieu et al[23] and Meier et al.[4] in which dayglow spectra were obtained between 530 and 1500 A. Meier et al presented a detailed analysis of prominent N_2 and N FUV emissions from this experiment. During FY84, we will determine the applicability of such coincident or near coincident data for establishing the relationship between optical emissions and the solar FUV spectrum.

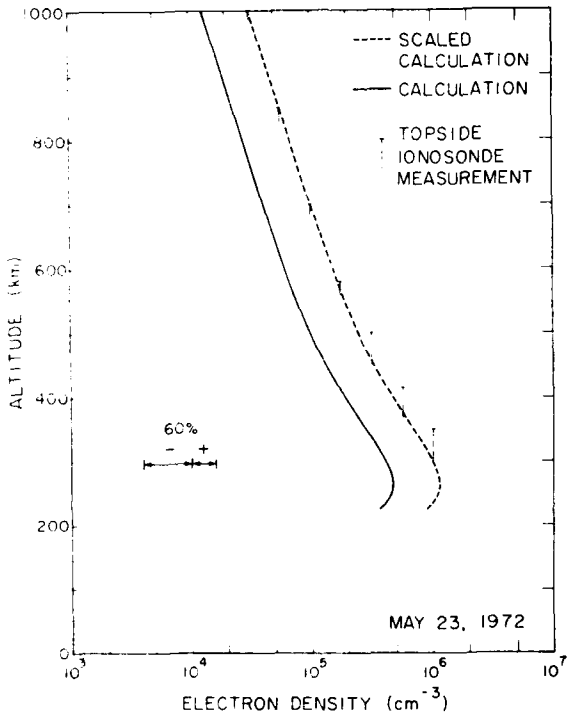

Figure 8. Daytime EDP's on 23 May 1972. The ISIS 2 topside sounder provided the measured profile. The solid curve is the calculated profile. The dashed curve has the calculated shape with its magnitude obtained by fitting to the data

21. Bowyer, S., Kimble, R., Parasce, F., Langston, M., and Penegor, G. (1981) Continuous readout airglow spectrometer, Appl. Optics, 20:477.

22. Huffman, R.E., LeBlanc, F.J., Larrabee, J.C., and Paulsen, D.E. (1980) Satellite vacuum ultraviolet airglow and auroral observations, J. Geophys. Res. 85:2201.

23. Gentieu, E.P., Feldman, P.D., and Meier, R.R. (1979) Spectroscopy of the extreme ultraviolet dayglow at 6.5 A resolution: Atomic and ionic emissions between 530 and 1240 A, Geophys. Res. Lett. 6:325.

4. NIGHTTIME MIDLATITUDE IONOSPHERE

Optical techniques for monitoring the EDP are particularly attractive when applied to the nighttime midlatitude ionosphere. Here, emissions are direct signatures of the height and magnitude of the EDP. These emissions come from radiative and ion-ion recombination ($O^+ + e \rightarrow O^*$; $O^+ + O^- \rightarrow O + O^*$) and from dissociative recombination ($O_2^+ + e \rightarrow O + O^*$). A key feature arising from the O^+ recombination processes is OI 1356A. The single useful feature from O_2^+ recombination is OI 6300 A (for nadir viewing conditions). We may relate their intensities respectively to the EDP maximum $N_m F_2$ and its location $h_m F_2$ by

$$\sqrt{4\pi I_{1356}} = g_1(N_m F_2)$$

and

$$\sqrt{\frac{4\pi I_{1356}}{4\pi I_{6300}}} = g_2(h_m F_2)$$

where $4\pi I$ is the column emission rate and g_1 and g_2 are functions dependent on the assumed shape of the EDP and the chemistry.[24, 25] Figures 9a and 9b show the important functional dependences within these equations. Here the EDP shape is given by a modified Chapman function, which generally characterizes the EDP reasonably well over the altitude range containing most of the TEC. The square root of the 1356 A intensity is very nearly proportional to $N_m F_2$ and insensitive to $h_m F_2$. The ratio of the square root of the 1356 A intensity to the 6300 A intensity is a sensitive function of $h_m F_2$ but nearly independent of $N_m F_2$. Note the log like dependence of $\sqrt{4\pi I_{1356}}/4\pi I_{6300}$ in Figure 9b. This dependence, especially for $h_m F_2 \sim 300$ km, is favorable for determining $h_m F_2$ even in the presence of likely levels of uncertainty in the intensities. A discussion of the processes leading to the dependences shown in Figures 9a and 9b is given in Appendix A.

---

24. Tinsley, B.A., and Bittencourt, J.A. (1975) Determination of F region height and peak electron density at night using airglow emissions from atomic oxygen, J. Geophys. Res., 80:2333.

25. Chandra, S., Reed, E.I., Meier, R.R., Opal, C.B., and Hicks, G.T. (1975) Remote sensing of the ionospheric F layer by use of OI 6300 A and OI 1356 A observations, J. Geophys. Res. 80:2327.

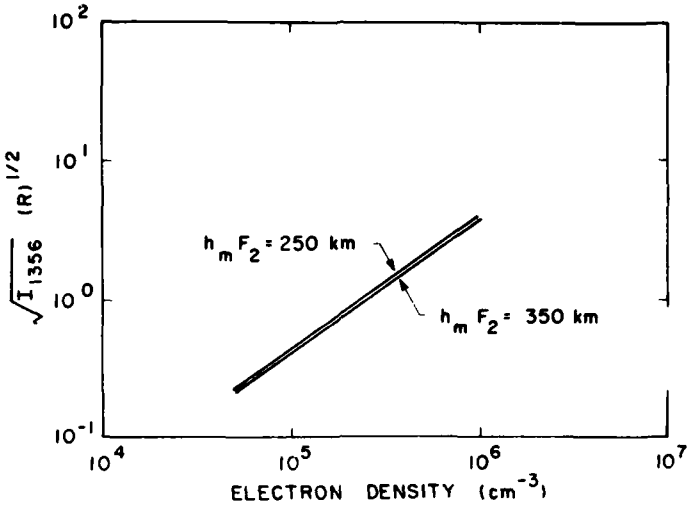

Figure 9a. The Dependence of the 1356 A Intensity on the Peak Electron Density, $N_m F_2$. The ordinate is the square root of the intensity. It is a linear function of $N_m F_2$ and has only a weak dependence on $h_m F_2$

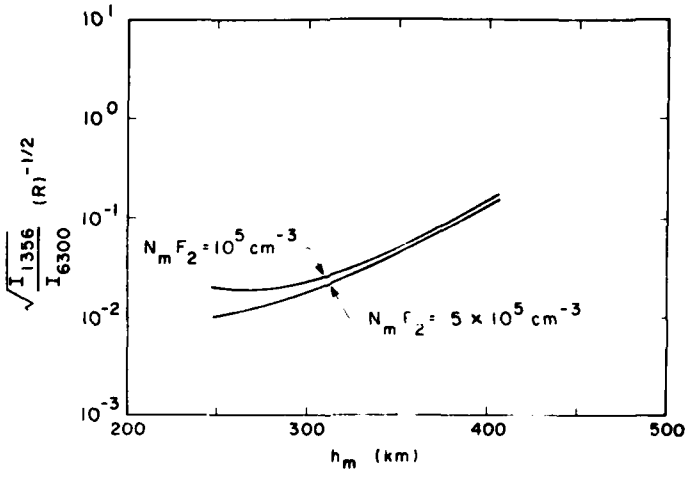

Figure 9b. The Dependence of the 6300 A Intensity on the Height of the Electron Density Peak, $h_m F_2$. The ordinate is the ratio of the square root of the 1356 A intensity to the 6300 A intensity

4.1 Properties of the Electron Density and Optical Emissions

The midlatitude ionosphere undergoes diurnal, seasonal, and solar cycle variations as well as irregular changes associated with magnetic storms. Latitudinal variations are relatively modest at middle latitudes, but geomagnetic disturbance effects are strongest in the high latitude range. The normal extremes in peak density are 5×10^4 cm^{-3} (usually just before dawn) and 10^6 cm^{-3} (usually just after sunset), with occasional excursions outside this range due to geomagnetic disturbances and solar activity. The height of the peak is almost always above 250 km during the night and commonly rises to 300-350 km near midnight (500 km at the equator).

Because the D, E, and F_1 regions are composed of molecular ions, they tend to disappear at night due to rapid recombination. A small E layer (generally less than 10^4 cm^{-3}) is maintained throughout the night by scattered EUV radiation.[26,27] The F_2 region is dominated by O^+ and is maintained by downward diffusion of O^+ from higher altitudes. These O^+ ions are lost due to charge exchange with molecular species below the peak. The peak occurs near the altitude where the time scale for vertical transport equals the chemical time scale.[26] Because vertical transport is significantly influenced by neutral winds, the variability of the F_2 peak is closely related to variability in the thermospheric circulation. For example, equatorward directed winds blow the plasma up along field lines. This produces not only a higher altitude for the F_2 peak but also a greater density at the peak because chemical loss rates decrease rapidly with increasing height due to decreasing neutral density (see, for example, Evans,[28] and Strobel and McElroy[17]). The reverse, of course, applies for poleward winds.

Of the emission features which can be used for ionospheric monitoring, the two most important are the atomic oxygen lines with wavelengths of 6300 A and 1356 A. We have developed a computer code which calculates the intensity of these features as they would be observed by a high altitude satellite (see Appendix A). Using the diurnal and seasonal variations displayed in Figure 10 and this computer code, we have calculated the corresponding variation in the emission features. The intensities as a function of local time are shown in Figure 11. Note that while the 6300 A intensity generally lies between 10 and 100 Rayleighs, the 1356 A intensity lies between 0.05 and 2 Rayleighs. The low end of the range of 1356 A intensities

---

26. Bauer, S. J. (1973) Physics of Planetary Ionospheres, Springer, New York, p. 183.

27. Schunk, R. W., and Nagy, A. F. (1980) Ionospheres of the terrestrial planets, Rev. Geophys. Space Phys. 18:813.

28. Evans, J. V. (1975) A review of F region dynamics, Rev. Geophys. Space Phys. 13:887.

is reached sometime during the night regardless of season. These values are for the worst case, solar minimum, and will generally be larger at solar maximum.

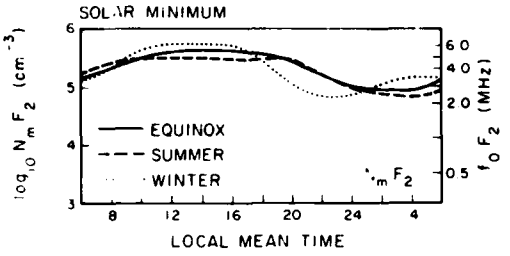

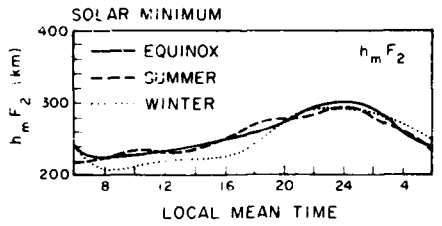

Figure 10. Comparison of the Diurnal Variation of the Peak Electron Density ($N_m F_2$) and Height of the Peak ($h_m F_2$) Over Millstone Hill for Summer, Winter, and Equinox Near Solar Minimum

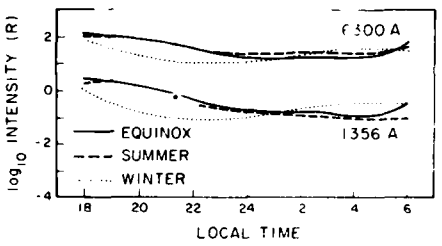

Figure 11. Local Time Variations of 6300 A and 1356 A Emissions for Summer, Winter, and Equinox Conditions. The calculated intensities are based on the electron density information in Figure 10

A representative latitudinal variation of the 6300 A and 1356 A intensities is shown in Figure 12. These were calculated using a representative ionospheric variation shown in Figure 13. For this particular example, the 6300 A intensity falls between 1 and 10 Rayleighs while the 1356 A intensity has about the same range as in Figure 11. Note that during a severe magnetic disturbance the 1356 A intensity near 50° geomagnetic latitude may be reduced by as much as a factor of 2. The reduction is much less at lower latitudes.

Thus a conservatively designed optical system intended for use as an ionospheric monitor must be capable of detecting as little as 1 Rayleigh of 6300 and 0.05 Rayleigh of 1356 A. Such a system is described in Appendix B.

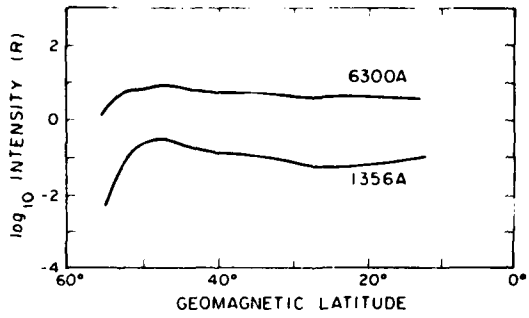

Figure 12. Latitudinal Variation of 6300 and 1356 A Emissions for Conditions Representative of the Post-midnight, Winter Ionosphere Near Solar Maximum. The calculated intensities are based on the electron densities of Figure 13

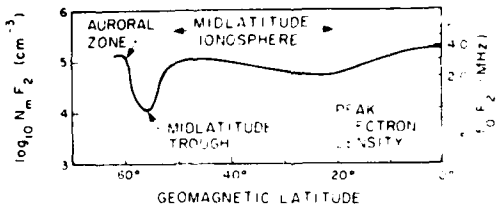

Figure 13. Latitudinal Variation of Peak Electron Density ($N_m F_2$) and the Height of the Peak ($h_m F_2$). The plot is representative of ionospheric conditions after midnight, in winter, and near solar maximum

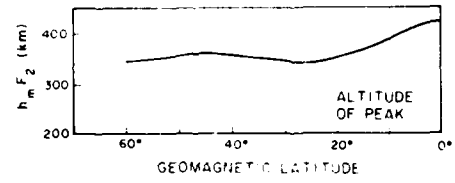

4.2 Comparison With Experiment

Although the general technique for relating airglow emission intensities to ionospheric parameters was first proposed in 1975, there have been relatively few attempts to verify the technique by comparing optical data with other measurements. Chandra et al[25] had trouble finding ionosonde measurements that were taken at the same time and place as their optical data but did find two cases in which the difference between bottomside sounder and optical data was quite good, being less than 15% for $N_m F_2$ and less than 15 km for $h_m F_2$. Recently Baumgardner and Mendillo[29] have used this technique (with the 7774 A feature instead of the 1356 A feature) to deduce total electron content near the geomagnetic equator. Meier and Opal[3] used satellite data for both the 1356 A and the 1304 A lines to verify that the intensity is proportional to the square of $N_m F_2$. Their values for $N_m F_2$ tended to be somewhat

29. Baumgardner, J., and Mendillo, M. (1983) Airglow imaging of ionospheric structures near the geomagnetic equator (Abstract), EOS, Trans. Am. Geophys. Union 64:275.

lower than ground based ionosonde data, although calibration and other problems made quantitative comparisons difficult.

Another comparison was done by Sahai et al[30] using ground based data. Instead of the OI 1356 A feature they used the atomic oxygen line at 7774 A. They determined $N_m F_2$ and $h_m F_2$ using both optical data and ionosonde data taken at the same time and location. In Figure 14 the values of $N_m F_2$ determined from optical data are plotted against the values determined from ionosonde data. The scatter indicates a statistical uncertainty of 10-15%, but the optical determinations are systematically 20% higher than the ionosonde measurements. The same situation applies to the comparison of the $h_m F_2$ determination and is illustrated by Figure 15. The statistical uncertainty appears to be 20-40 km while the systematic errors are 20-30 km, that is, their optical data did track ionospheric variations quite well, although a calibration correction was wanting.

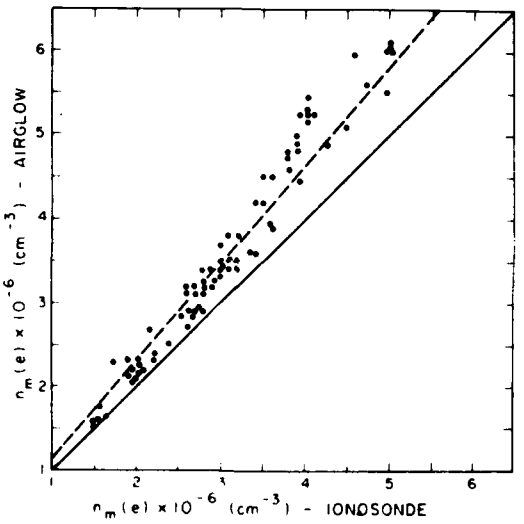

Figure 14. Plot of $N_m F_2$ Deduced From Optical Data (airglow) Against $N_m F_2$ From Ionosonde Data

30. Sahai, Y., Bittencourt, J.A., Teixeira, N.R., and Takahashi, H. (1981) Simultaneous observations of OI 7774 A and OI 6300 A emissions and correlative study with ionospheric parameters, J. Geophys. Res. 86:813.

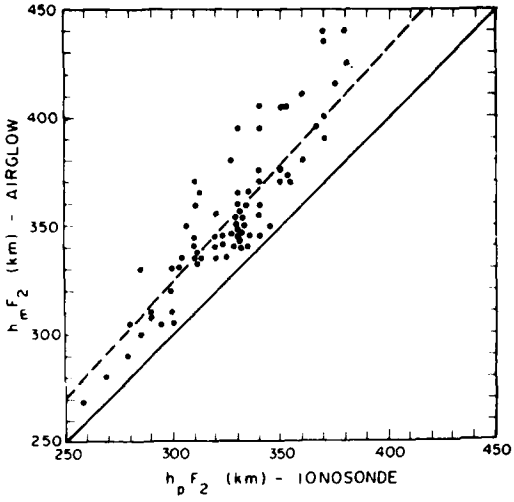

Figure 15. Plot of $h_m F_2$ Deduced From Optical Data (airglow) Against $h_m F_2$ Ionosonde Data

We have carried out a number of simulated data analyses based on incoherent scatter radar data from Millstone Hill (57° N geometric latitude) and Arecibo (29° N geomagnetic latitude). We use the radar data to determine the actual EDP, the direct code (see Appendix A3) to calculate the optical emissions expected from that EDP, and the inverse code to deduce $N_m F_2$ from the optical emissions. An example of this calculation is shown in Figure 16. The observed profile is a midnight profile from Evans.[18] The exospheric temperature is 800 K. The optical intensities calculated by the direct code are 5.3 Rayleighs of 1356 A and 23.9 Rayleighs of 6300 A. From these intensities, the inverse code calculated $N_m F_2$ to be 6.3×10^5 cm^{-3} and $h_m F_2$ to be 338 km. The actual values are 6.4×10^5 cm^{-3} and 349 km, respectively (see Figure 16). The total electron content (TEC) calculated from the model is 7% less than the value calculated from observations.

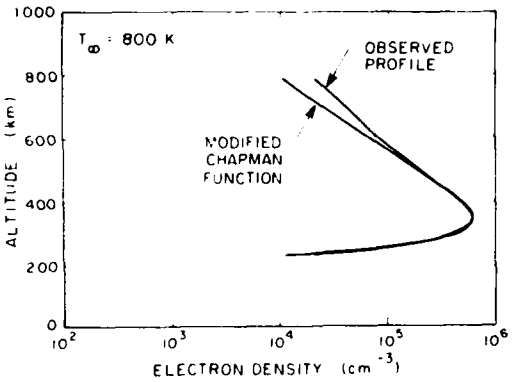

Figure 16. A Comparison of an Observed Electron Density Profile From Millstone Hill and the Profile Calculated by the Inverse Nighttime Code

The contour plots of Figure 17 illustrate a major challenge to any ab-initio modeled EDP calculation: a common major nighttime transport event. During summer, the lower mid-latitudes show significant decreases in the EDP height and magnitude on many but not all nights near midnight. The contour plots for the three nights of Figure 18 are illustrative of the normal night-to-night variability. This variability leads to departure of the EDP from state-of-the-art models that can be a factor of 5-10! We have applied our direct and inverse codes to some of these data to see if they reproduce the observed EDP during major transport events.

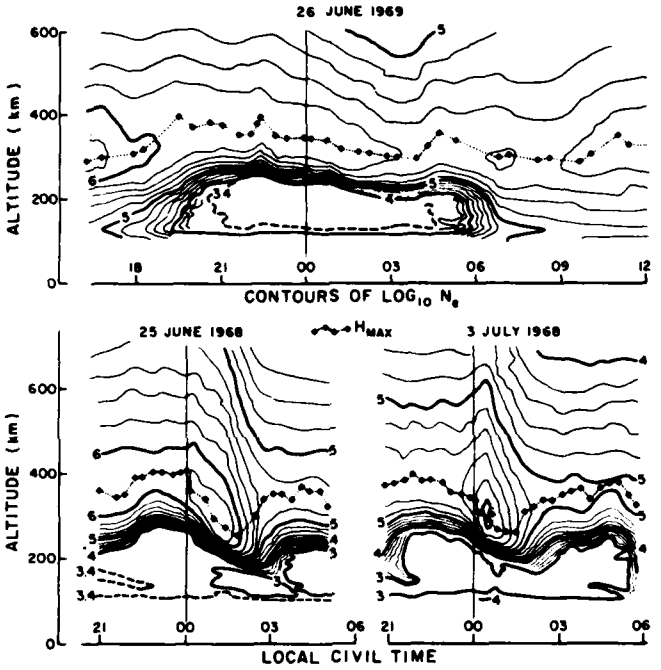

Figure 17. Contours in Log_{10} of Electron Concentration (electrons cm^{-3}), on an Altitude vs Local Time Grid, Showing Patterns of Behavior in the Nighttime Mid-latitude Ionosphere Over Arecibo at 18.3° N Geographic (29° N magnetic) Latitude. Equatorward neutral winds are important in maintaining the nighttime ionosphere as in the upper half of the figure. Transient poleward wind components of unknown origin generally sweep across the entire midlatitude sector of the globe, manifested here by rapid order-of-magnitude drops in topside plasma concentrations and transient bottom-side increases of two to three orders of magnitude (from Hanson and Carlson[45])

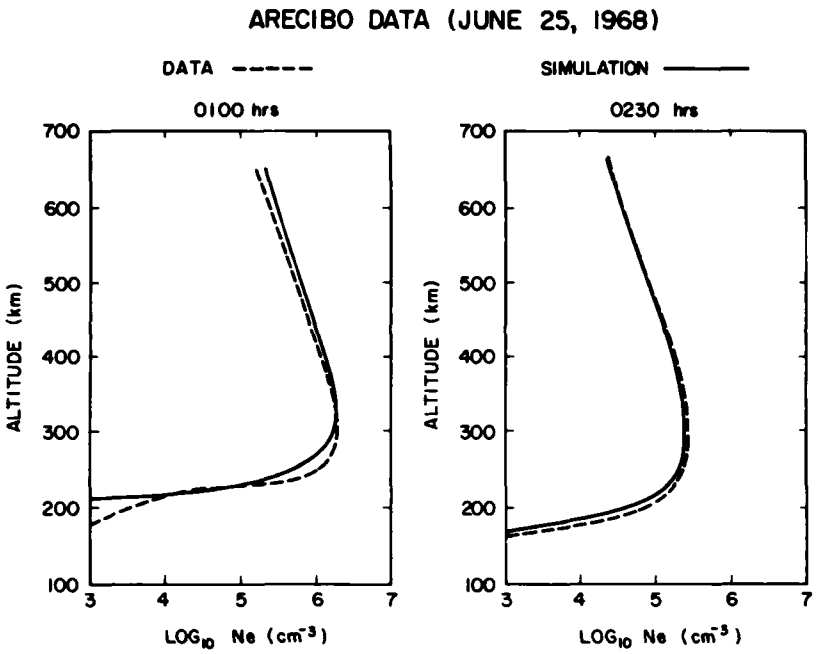

Figure 18. Calculated and Observed EDP's at 0100 and 0230 Local Time on 25 June 1968. The observed EDP comes from Figure 17. The calculated EDP is based on 1356 A and 6300 A intensities derived from the observed EDP

Figure 18 shows the calculated and observed EDP at the peak of the transport event (0230 local time) on 25 June 1968. By contrast to conventional models that have been in error by about a factor of 8, our model EDP as based on the pair of optical emission lines agrees within roughly 20%, a striking improvement. Generally, we are exploring first order refinements to the Chapman EDP shape function based on the optical emissions for major transport events. Although our investigation has not been exhaustive, a number of simulations for a variety of ionospheric conditions produce similar results. Generally the deduced values of $N_m F_2$ are within 15% of the observed values, $h_m F_2$ within 25 km, and TEC within 10%.

Although present understanding of ionospheric and airglow processes indicates that the basic technique is sound, questions concerning implementation of the technique remain to be explored in FY84-85. These include some aspects of the background problem (discussed in Appendix B), precise values for reaction rates, the validity of the Chapman function representation, and the need for accurate models of the neutral atmosphere. Some of these questions can be answered by studying data that are already available, but a comprehensive comparison of optical data

with topside and bottomside sounder data and incoherent scatter radar data will also be required. This comparison will ensure that the optical data can be used to infer ionospheric parameters with a minimal loss of accuracy. An analysis of the achievable accuracy of a specific detection system is given in Appendix B. A discussion of various operational considerations of this system is given by Appendix C.

5. THE AURORA

We can state with some confidence that the auroral E-region electron density profile can be determined to an accuracy of ± 30% if we know the precipitating electron spectrum and if the precipitation is reasonably constant on a time scale of a minute or more. This statement is based on data analyses discussed in Section 5.3. The problem we face is determining this spectrum from satellite optical data. There is no serious problem determining the incident energy/cm^2-s from overall brightnesses of selected intensities. This is valuable in itself since a good estimate of n_e^{max} in the E region can be made using this information with the aid of models. The shape of n_e, however, is sensitive to how the energy is distributed over the electron spectrum. Our recent work has focused on how well this spectrum can be determined from relative brightnesses among a variety of FUV and EUV features. This issue is addressed in a quantitative way by Strickland et al.[31]

There are no useable direct optical signatures of n_e in the auroral E-region. This is because most of the emission in any feature is caused by electron impact on neutral species. This is to be contrasted to the nighttime optical emission discussed in Section 4 which provide direct signatures of n_e. There is the possibility of obtaining auroral F region n_e information directly from OII 834 A. This would be done by obtaining limb or near limb 834 A intensity profiles. The shape of such profiles is affected by the amount of O^+ present through multiple scattering of the 834 A photons. The technique is probably not useful for auroral applications because of the typical degree of horizontal structure present in the emission. Our comments here will be restricted to the E region.

We have been investigating the auroral E region over the past few years using a coupled electron transport/chemistry/optical emission model for predictions and rocket/satellite data analysis. We have discovered measurable changes in calculated intensities among various NUV, FUV, and EUV features resulting from

31. Strickland, D.J., Jasperse, J.R., and Whalen, J.A. (1983) Dependence of auroral FUV emissions on the incident electron spectrum and neutral atmosphere, J. Geophys. Res. 88:8051.

changes in the precipitating electron spectrum. We have further observed changes exceeding a factor of 4 in STP 78-1 EUV data among selected features. This has been reported in Quarterly Report 2 on contract F19628-83-C-0078. It is now clear that accurate measurements of selected intensities will yield information on the electron spectrum. We are not yet able to state to what accuracy the spectrum can be characterized. This will be done once the needed optical system is placed on a satellite also carrying an electron spectrometer.

5.1 Electron Density and Optical Emissions

The purpose of this Section is to provide background information to the reader not acquainted with the auroral observables of interest to this program. Observed and calculated electron densities as well as optical intensities will be presented. We wish to stress that great variability exists in the energy dependence of precipitating electron spectra along with energy content, duration of the precipitation, and spatial extent. We will not address the variability issue in this subsection. Our intent is one of orientation in which examples of the observables will be given. Emphasis will be placed on the E region for which our models have been well tested.

We begin with examples of Φ_o, the precipitating electron spectrum. Figure 19 shows three spectra obtained with the electron spectrometer onboard DMSP F-2 (see Hardy et al[32] for a description of the instrument). These spectra were recorded within seconds of one another as the satellite passed through the continuous aurora. They were selected for display because we are using them (along with numerous others) in an analysis of F-layer plasma enhancements. The investigation, under the direction of Dr. E. J. Weber of AFGL, is considering coordinated measurements using the Chatanika radar facility, DMSP F-2, and the AFGL Airborne Ionospheric Observatory. Findings from this work will be reported elsewhere.

The spectra in Figure 19 are characteristic of those producing the continuous aurora. They possess a Maxwellian character above several hundred eV. As mentioned above, there is great variability in auroral spectra for which a large body of published literature exists. For the sake of brevity in this subsection, we choose not to discuss this extensive subject.

---

32. Hardy, D.A., Gussenhoven, M.S., and Huber, A. (1979) The Precipitating Electron Detectors (SSJ/3) for the Block 5D/Flights 2-5 DMSP Satellites: Calibration and Data Presentation, AFGL-TR-79-0210.

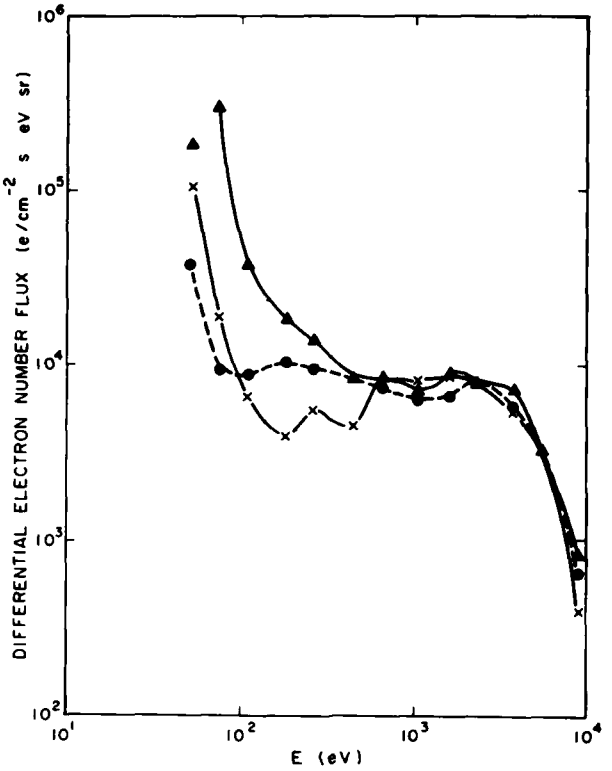

Figure 19. DMSP F-2 Data (Hardy et al[32]). All data were recorded within a 3-sec interval as the satellite was passing through the continuous aurora

Examples of calculated E region electron density profiles are shown in Figure 20 and come from Strickland et al.[31] The left panel shows the total ionization rates while the densities appear on the right. The precipitating electron spectra were characterized by Gaussians with characteristic energies from 1 to 10 keV. The energy content of all spectra was 1 erg/cm^2-s. The chemistry rate equations were integrated in time until chemical equilibrium was achieved.

A measured electron density profile is shown in Figure 21. The profile was taken from a map being used in the F region plasma enhancement study mentioned above. The map was generated with Chatanika incoherent radar data. Below 200 km is the auroral E-layer produced by precipitating electrons having spectral characteristics like those shown in Figure 19. The profile has been displayed to 400 km to include the F peak. The exhibited F region behavior is not unique for the given

E region profile. Weber et al[33] have reported data showing significant F-region plasma enhancements during times when electron precipitation is not markedly changing. F-region plasma convection is the cause of such behavior.

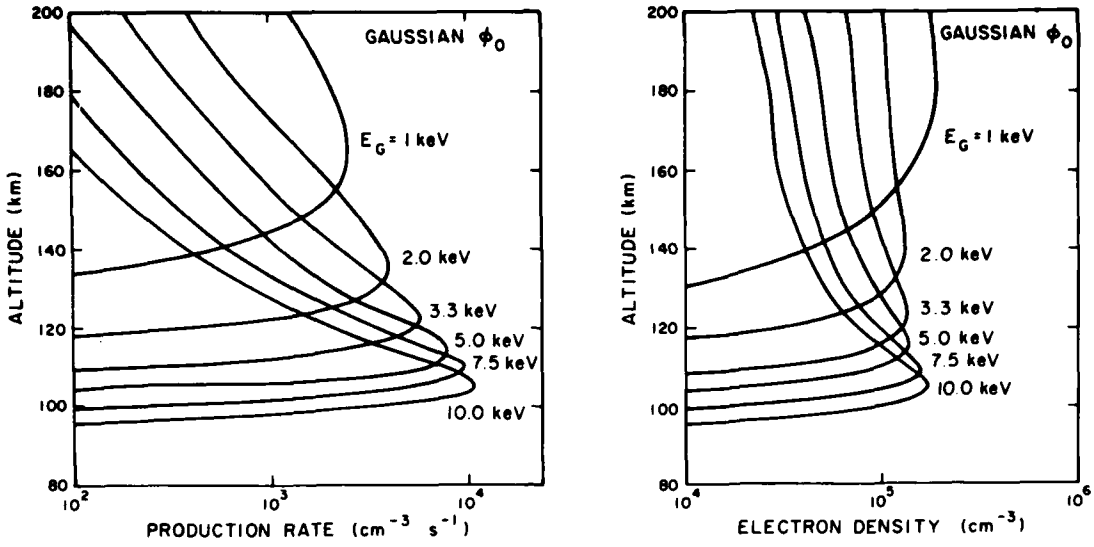

Figure 20. Total Ion Production Rates and Electron Densities for Precipitating Electron Spectra Given by Gaussian Distributions With Energy Contents of 1 erg/cm^2-s

The remaining observables to be discussed are optical intensities. Figure 22 shows an auroral FUV spectrum obtained from a rocket experiment with the spectrometer viewing downward near apogee. (P. D. Feldman, private communication, 1981.) The most prominent features are various N_2 LBH bands, NI 1200 A, HI 1216 A, OI 1304 A, and OI 1356 A. An indication of the nature of the auroral EUV spectrum may be obtained from Figure 6 previously introduced in Section 3. Actual auroral spectra are given in Paresce et al[34] for day and night auroras. As in the daytime, these spectra contain numerous lines of OI, OII, NI, and NII. Table 2, previously introduced in Section 3 lists the optical features spanning the FUV and EUV regions under investigation by us.

33. Weber, E.J., Buchau, J., Moore, J.G., Sharber, J.R., Livingston, R.C., Winningham, J.D., and Reinisch, B.W. (1983) F-layer ionization patches in the polar cap, J. Geophys. Res. (in press).

34. Paresce, F., Chakrabarti, S., Bowyer, S., and Kimble, R. (1983) The extreme ultraviolet spectrum of dayside and nightside aurora: 800-1400 A, J. Geophys. Res. 88:4905.

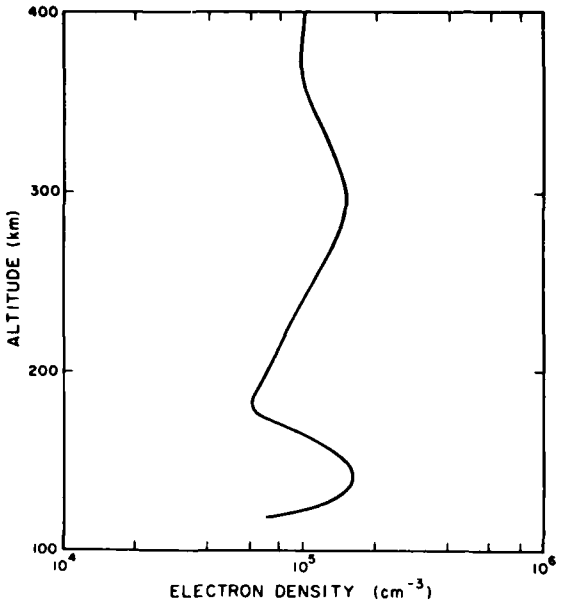

Figure 21. Electron Density Profile Obtained With the Chatanika Radar System. The E region was produced by the continuous aurora

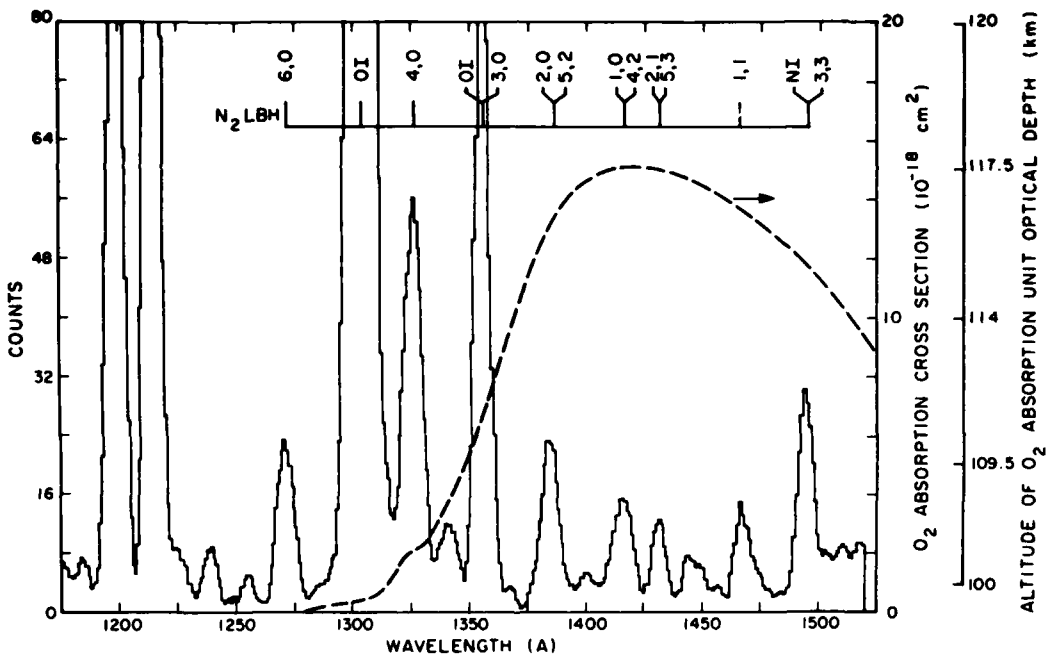

Figure 22. An Auroral FUV Spectrum From P. D. Feldman (private communication) Obtained in a Rocket Experiment With the Spectrometer Looking Down From Above the Emitting Region. Dashed curve gives O_2 photo absorption cross section. Altitude scale on right is to be used with adjacent cross section scale

The auroral spectra in Paresce et al[34] reveal significant changes from day to night. Such changes are caused by charges in the precipitating electron spectrum and possibly by atmospheric changes. This is discussed in detail by Strickland et al.[31] An important process behind spectral variability in the EUV and FUV regions is pure photon absorption by O_2 which varies in strength from feature to feature.

The existence of spectral variability provides the means of estimating precipitating electron spectra and the altitude profiles of O and O_2 densities relative to the N_2 density. We have been examining the variability or equivalently, the relative behavior of the nadir intensity of one feature relative to another using our combined model of electron transport, chemistry, and optical emissions. An example of such behavior is shown in Figure 23 taken from Strickland et al.[31] Selected FUV nadir intensities are shown as a function of E_G, the characteristic energy of the precipitating electron spectrum which has been characterized by a Gaussian distribution. For all E_G values, the energy content is 1 erg/cm^2-s. The primary cause of the variations shown is O_2 pure absorption.

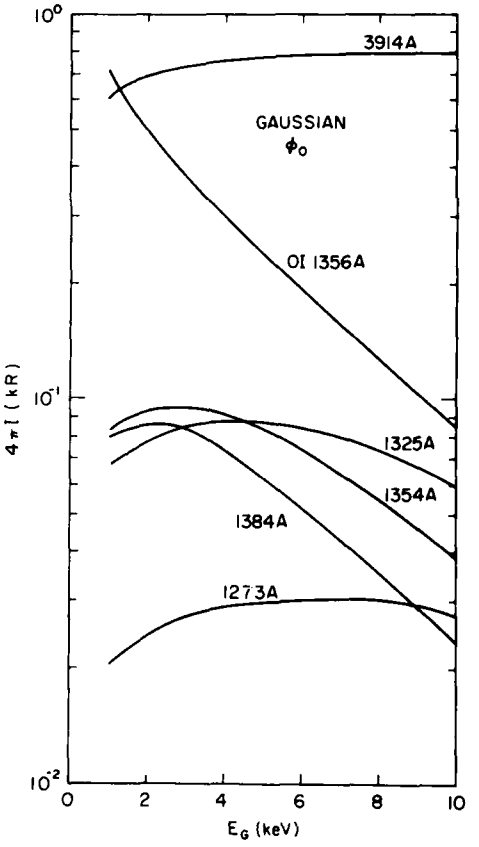

Figure 23. Nadir Intensities for Precipitating Electron Spectra by Gaussian Distributions With Energy Contents of 1 erg/cm^2-s. E_G is the characteristic energy

5.2 Approach

We wish to describe the interaction of auroral electrons with the atmosphere, the time evolution of chemical species, and the emission properties of various lines and band emission features. Our interest is in relating intensities as observed from a satellite to the electron density. We have at our disposal a series of codes which we group under the two descriptors B3C and CHEM. B3C stands for Boltzmann 3 Constituent where 3C refers to N_2, O_2, and O, the species primarily responsible for the particle-particle interactions experienced by the electrons. Code B3C solves a Boltzmann electron transport equation in matrix form giving $\Phi(z, E, \mu)$, the electron spectrum as a function of altitude z, energy E, and direction cosine μ. B3C also evaluates volume excitation and ionization rates $p_i(z)$ needed for chemistry modeling. The publication by Strickland et al[35] describes the B3C model. Code CHEM solves a set of coupled rate equations for neutral and ion densities as a function of time. The electron density is given by summing the ion densities. The code also calculates altitude profiles of nadir and zenith intensities for a variety of line and band emission features such as those listed in the previous subsection. An application of codes B3C and CHEM is described in the recent publication by Strickland et al[31] which addresses the issue of using satellite observed intensities to monitor the auroral ionosphere.

Figure 24 shows a flow diagram illustrating inputs to and outputs from codes B3C and CHEM. Table 3 lists the chemical species presently treated in the model. The cross sections used in B3C describe elastic scattering and discrete energy loss. Those used in CHEM refer to specific emission processes. An integration of an emission cross section times $\Phi(z, E)$ (Φ integrated over 4π) times the impacting density gives a volume emission rate which when integrated over altitude gives $4\pi I$, the apparent column emission rate. Pure absorption effects are included in the altitude integration. The quantity I by itself is the intensity in photons/cm^2-s-sr. It is common practice to convert optical observations to $4\pi I$ having units of Rayleighs. As shown in Figure 24, code CHEM provides emission in the form of $4\pi I$ which has the Rayleigh unit. The quantity Φ_o shown as an input to B3C is the precipitating electron spectrum incident at the upper boundary of the scattering medium. It is specified over the downward hemisphere. The spectrum at this boundary over the upward hemisphere is part of the solution $\Phi(z, E, \mu)$. The densities n_i shown as outputs from CHEM refer to those species listed in Table 3.

---

35. Strickland, D. J., Book, D. L., Coffey, T. P., and Fedder, J. A. (1976) Transport spectrum of dayside and nightside aurora: 800-1400 A, J. Geophys. Res. 81:2755.

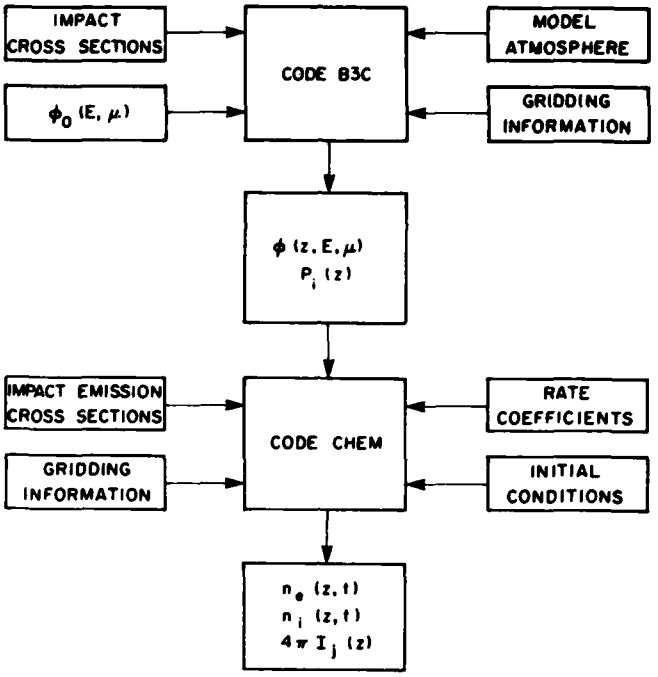

Figure 24. Inputs and Outputs for Auroral Electron Transport Code B3C and Chemistry/Emission Code CHEM

Table 3. Chemical Species Presently Modeled in Code CHEM

Species	
NO^+	NO
O_2^+	$N(^4S)$
O^+	$N(^2D)$
N_2^+	$O(^1D)$
N^+	$O(^1S)$
$O^+(^2D)$	$N_2(A\ ^3\Sigma)$
$O^+(^2P)$	$O_2(a\ ^1\Delta)$
$O_2^+(a\ ^4\Pi)$	$O_2(b\ ^1\Sigma)$

5.3 Comparison With Experiment

The calculation of auroral electron spectra, excitation rates, chemical species densities, and optical intensities involves a large body of input data and the use of large computer codes. It is essential to compare these calculated quantities with independent results as well as measurements prior to a serious investigation of the problem being addressed.

Electron spectra are the most difficult to calculate of the above mentioned quantities. We have tested them through various comparisons and by observing how well they conserve energy. The latter test typically yields an error of less than 10%. The auroral electron results have been well tested beginning with comparisons discussed by Strickland et al,[31] followed by subsequent comparisons with rocket and satellite data. This latter work is unpublished but does generally show good agreement. Specific examples of applied data are the rocket data of Spiger and Anderson[36] and satellite data of Craven and Frank.[37] The observed quantity is the auroral electron spectrum given as a function of both energy and angle.

We have compared calculated ion densities and optical intensities with similarly measured quantities reported by Rees et al[38] and Sharp et al.[39] The comparisons have been documented by Strickland.[40] The data come from a rocket experiment which provided altitude profiles of the densities and intensities as well as the spectrum of precipitating electrons. Agreement between intensities was better than 10% for viewing through the entire emitting region. Agreement between electron densities was better than 30% throughout most of the E region (see Figures 13 and 15 in Strickland[40]).

We have also compared our calculated quantities with data obtained from the AFGL auroral E rocket program conducted on 7 March 1981. Since this has not been documented elsewhere, a brief description of the analysis will be given here. Four rockets were launched from the Poker Flat Research Range near Fairbanks, Alaska into the continuous aurora. Observations were made of particles, fields, and optical emissions. The AFGL Airborne Ionospheric Laboratory and Chatanika Radar System were also operating during the evening of the launches.

We will show comparisons with n_e obtained from the radar data (Robinson and Vondrak[41]) relative ion concentrations obtained with a mass spectrometer (Swider and Narcisi[42]) and intensities obtained with photometers (Van Tassel[43]). Other data deserving comment are primary electron and FUV spectrometer data. The electron spectrometer experienced some difficulty which prevents us from making a meaningful comparison with its data. We are in possession of the FUV data but in a preliminary form. Presentation of comparisons with these data will be postponed until we receive a final version.

(Due to the large number of references cited above, they will not be listed here. See References, page 51.)

We know the approximate spectral behavior of precipitating electrons producing the continuous aurora (see Whalen[44]). A Maxwellian distribution effectively characterizes this spectrum above several hundred eV where nearly all energy resides. We have carried out calculations for a series of Maxwellian distributions with various energy contents and determined a best distribution from fitting the data mentioned above. The E_o and Q_o values for that distribution are 1.3 keV and 2 ergs/cm^2-s where E_o is the characteristic energy and Q_o is the energy content. The precision we assign to these values is ± 15%, that is, we can probably obtain equally good fits to the electron density and optical data using other values of E_o and Q_o within this range by adjusting input data such as the model atmosphere and the low energy portion of $\Phi_o(E, \mu)$. Figure 25 shows the chosen incident spectrum and calculated spectrum at lower altitudes. Note that the spectra represent spherical fluxes, that is, $\Phi(z, E, \mu)$ has been integrated over 4π. Thus, the spectrum shown at 300 km (the chosen upper boundary) contains both the given incident part and the calculated emergent part.

Figure 26 shows calculated and measured relative ion concentrations for NO^+, O_2, O_2^+, N_2^+, and N^+. The figure was taken from Swider and Narcisi[41] to which we have added the calculated results. Agreement with the dominant species densities is within 10%. Figure 27 shows the calculated $n_e(z)$ and the corresponding quantity obtained with the radar (Robinson and Vandrak[41]).

Figure 28 presents zenith intensities for N_2^+ 1N 3914 A, N_2 2P 3371 A, and N_2 VK 2762 A (Vegard-Kaplan). The data were obtained with photometers (Van Tassel[43]) and occur in pairs showing the recorded profiles during rocket ascent and descent. The 3371 A feature also contains a contribution from N_2 VK 3353 A which has been included in our result. The calculation of VK emissions is not simple because of (1) cascading from $N_2(B)$, $N_2(C)$, $N_2(w)$, and possibly other states, (2) quenching of the $N_2(A)$ state, and (3) the general problem of transitions among vibrational levels. We defer a discussion of these issues to a paper in progress on auroral NUV emissions. The agreement in Figure 28 is seen to be good with differences of less than 20% over most of the altitude range.

---

44. Whalen, J.A. (1981) General characteristics of the auroral ionosphere, in physics of space plasmas, SPI Conf. Proc. Reprint Ser., 4, Ed. by T.S. Chang, B. Coppi, and J.R. Jasperse, Scientific Publishers, Cambridge, Massachusetts.

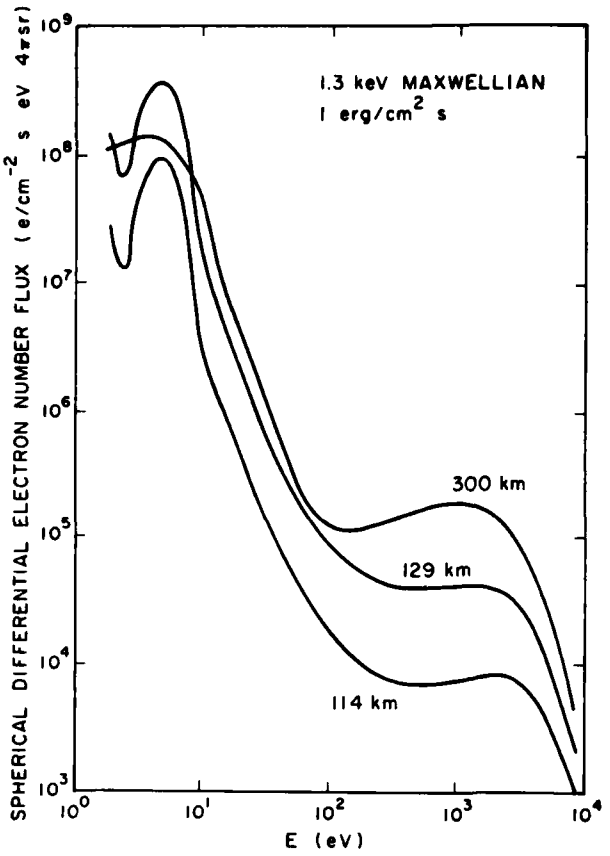

Figure 25. Calculated Electron Spectra Integrated Over 4π. A 1.3 keV Maxwellian with isotropy over the downward hemisphere defines the incident spectrum. Note that these results apply to an incoming power density of 1 erg/cm^2-s whereas the calculated electron density and column emission rates in Figures 27 and 28 apply to twice this value

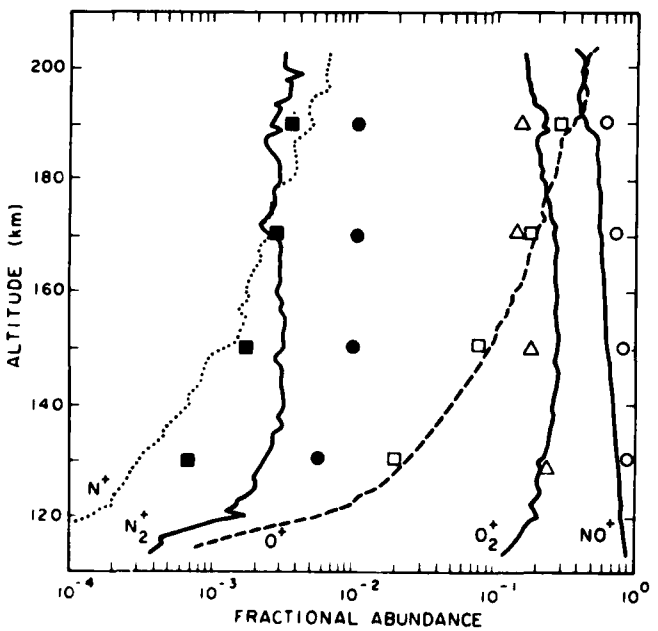

Figure 26. Calculated (symbols) and Measured (curves; Swider and Narcisi[42]) Fractional Ion Abundances

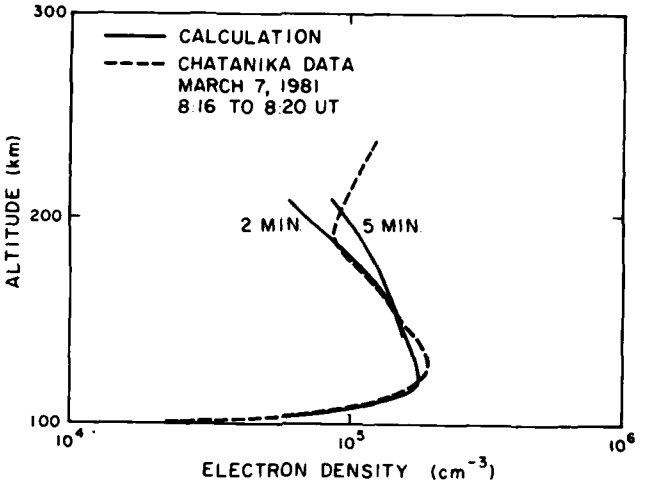

Figure 27. Observed and Calculated Electron Density Profiles for the 1981 AFGL Auroral E Rocket Program. Data come from Robinson and Vondrak.[41] A 1.3 keV Maxwellian containing 2 ergs/cm^2-s was used to characterize the incident electron spectrum in the calculation

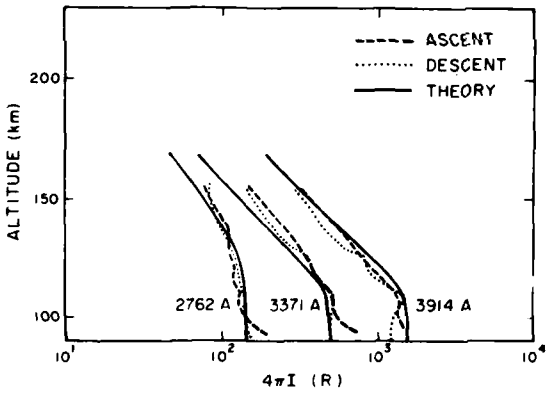

Figure 28. Observed and Calculated Column Emission Rates for the 1981 AFGL Aurora E Rocket Program.[43] Data come from Van Tassel. A 1.3 keV Maxwellian containing 2 ergs/cm^2-s was used to characterize the incident electron spectrum in the calculation

5.4 Discussion of Error

We will give examples of error bars for a specific set of circumstances. Otherwise, this discussion would become lengthy because of the large parameter space involved. Let us assume we know the N_2, O_2, and O densities and that the precipitating electron spectrum has a Gaussian behavior. Similar results would be obtained for other assumed distributions such as Maxwellians. We must now

choose emission features for deducing the hardness of the incident electron spectrum. Let these be 1356 A (OI 1356 A and LBH 1354 A) and LBH 1325 A. Their nadir intensities ($4\pi I$) vs E_G were given in Figure 23. Define r to be

$$r = \frac{4\pi I_{\text{OI 1356 A}} + 4\pi I_{\text{LBH 1354 A}}}{4\pi I_{\text{1325 A}}} .$$

Figure 29 shows r vs E_G for Q values of 1 and 10 ergs/cm^2-s (Q is rate of incoming energy of the incident spectrum). The shaded regions give 1σ error bars due to statistical uncertainty in the instrumental counting rate. The conversion from Rayleighs to counts/s applies to the spectrometer discussed by Huffman et al.[22]

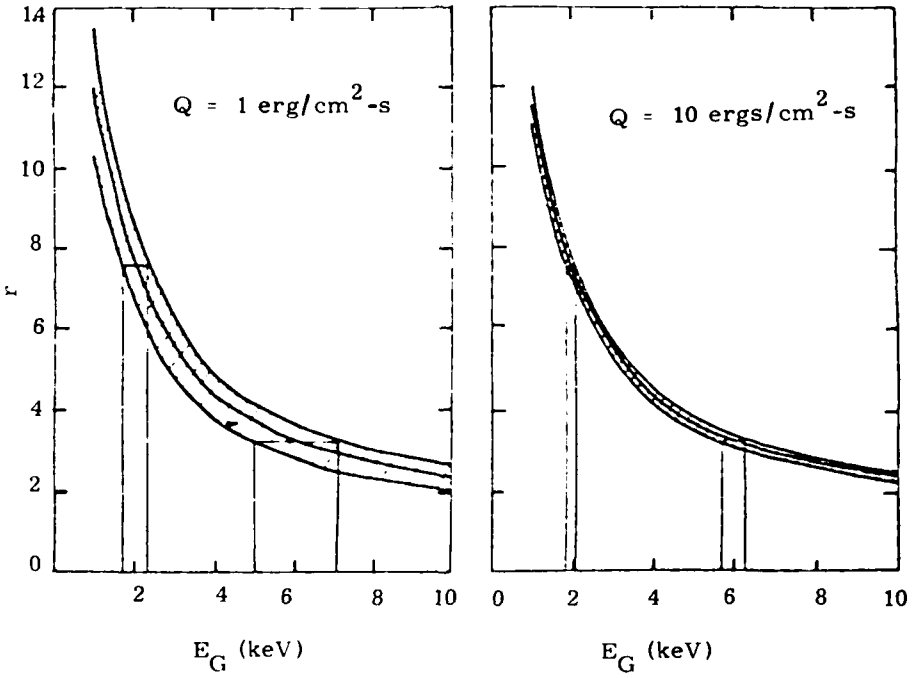

Figure 29. Nadir Intensity r vs E_G. The 1σ errors in E_G are shown for observed r values of 7.6 and 3.2

For illustration, let us consider the uncertainty in E_G for Q = 1 erg/cm^2-s and observed r values of 7.6 and 3.3. These give E_G values of 2 and 6 keV. The ranges of uncertainty are 1.7 - 2.3 keV and 5 - 7.1 keV. Figure 30 shows the resulting uncertainty in the EDP's for the two r values. Large uncertainty exists on the bottom side of these profile as expected for the rapid decreases below the peaks. Near the peaks and on the top side, the errors are typically better than ± 20%.

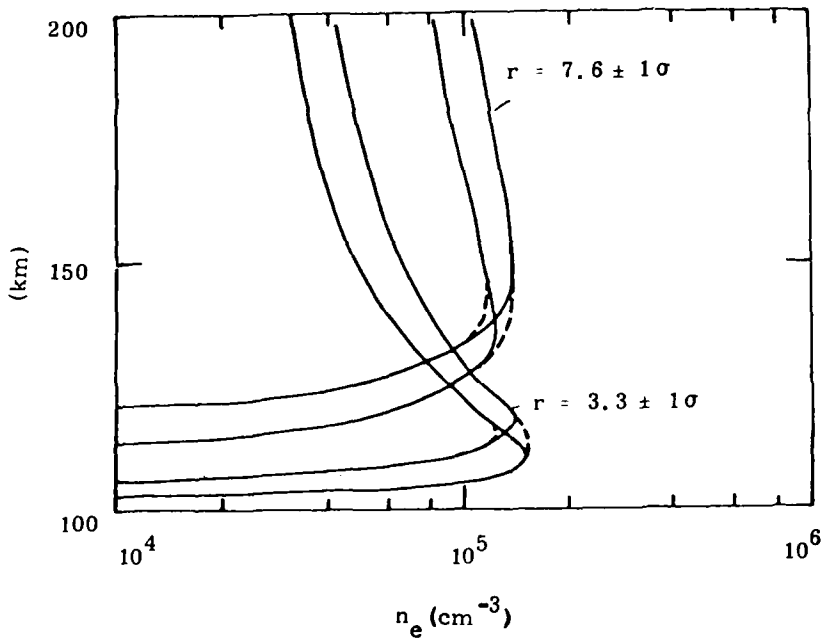

Figure 30. Range of Uncertainty in the EDP for the Uncertainties in E_G Shown in Figure 29. The EDP's are interpolated values based on the calculated profiles in Strickland et al[31]

One must be cautious in making general statements based on the limited error analysis carried out to date. Results such as those in Figure 30 are sensitive, for example, to the chosen features. We have not necessarily used the best ones at all energies, especially above several keV. The features are certainly attractive at lower energies, given the steep rise shown in Figure 29. A key issue we have not addressed is the accuracy we can expect in the N_2, O_2, and O densities, especially the O density. The ratio shown in Figure 29 is sensitive to variations in this density.

We plan an expanded error analysis this year in which results like those just shown will be generated for variations in the important parameters. These parameters are

(1) the neutral densities,
(2) the incident spectrum (Maxwellian as well as Gaussian dependence)
(3) intensity brightness,
(4) features defining r,
(5) duration of the precipitation, and
(6) instrument sensitivity.

References

1. Muldrew, D. B. (1965) F-layer ionization troughs deduced from Alouette data, J. Geophys. Res. 70:2635.
2. Fejer, B.G., and Kelley, M.C. (1980) Ionospheric irregularities, Rev. Geophys. Space Phys. 18:401.
3. Meier, R.R., and Opal, C.B. (1973) Tropical UV arcs: Comparison of brightness with f_oF_2, J. Geophys. Res. 78:3189.
4. Meier, R.R., Strickland, D.J., Feldman, P.D., and Gentieu, E.P. (1980) The ultraviolet dayglow, 1. Far UV emissions of N and N_2, J. Geophys. Res. 85:2177.
5. Meier, R.R., and Conway, R.R. (1983) On the N_2 Lyman-Birge-Hopfield band nightglow, J. Geophys. Res. 88:4929.
6. Heroux, L., Cohen, M., and Higgins, J.E. (1974) Electron densities between 110 and 300 km derived from solar EUV fluxes of August 23, 1972, J. Geophys. Res. 79:5237.
7. Heroux, L., and Hintereggar, H.E. (1978) Aeronomical reference spectrum for solar UV below 2000 A, J. Geophys. Res. 83:5305.
8. VanTassel, R.A., McMahon, W.I., and Heroux, L. (1981) Rocket Data of Solar EUV Flux Thermospheric Electron Flux and N_2 Second Positive Airglow Emission, AFGL-TR-81-0111, AD A104384.
9. Wadzinski, H.T., and Jasperse, J.R. (1982) Low Energy Electron and Photon Cross Sections for O, N_2, and O_2, and Related Data, AFGL-TR-82-0008, AD A118921.
10. Johnson, C.Y. (1969) Annals of the IQSY 5:197, (Strickland, A.C., Ed.) (1969) MIT Press, Cambridge, Massachusetts.
11. Jacchia, L.G. (1977) Thermospheric Temperature, Density and Composition: New Models, Smithsonian Astrophysical Observatory Special Report 375.
12. Takacs, P.Z., and Feldman, P.D. (1977) Far ultraviolet atomic and molecular nitrogen emissions in the dayglow, J. Geophys. Res. 82:5011.

References

13. Chakrabarti, S., Parasce, F., Bowyer, S., Kimble, R., and Kumar, S. (1983) The extreme ultraviolet day airglow, J. Geophys. Res. 88:4898.

14. Jasperse, J.R. (1976) Boltzmann-Fokker-Planck model for the electron distribution function in the earth's ionosphere, Planet. Space Sci. 24:33.

15. Jasperse, J.R. (1977) Electron distribution function and ion concentrations in the earth's lower ionosphere from Boltzmann-Fokker-Planck theory, Planet. Space. Sci. 25:743.

16. Anderson, D.N. (1973) A theoretical study of the ionospheric F region equatorial anamoly, I, Theory, Planet. Space Sci. 21:409.

17. Strobel, D.F., and McElroy, M.B. (1970) The F2-layer at middle latitudes, Planet. Space Sci. 18:1181.

18. Evans, J.V. (1976) The dynamics of the ionosphere and upper atmosphere, in Physics of Solar Planetary Environments, D.J. Williams, Ed., American Geophysical Union, Washington, 630.

19. Klumpar, D.M., Ed. (1980) Coordinated Ionospheric and Magnetospheric Observations from the ISIS 2 Satellite by the ISIS 2 Experimenters, 3, (NSSDC/WDC-A-R+S, 80).

20. Hinteregger, H.E., Bedo, D.E., and Manson, J.E. (1973) The EUV spectral photometer on atmospheric explorer, Radio Sci. 8:349.

21. Bowyer, S., Kimble, R., Parasce, F., Langston, M., and Penegor, G. (1981) Continuous readout airglow spectrometer, Appl. Optics, 20:477.

22. Huffman, R.E., LeBlanc, F.J., Larrabee, J.C., and Paulsen, D.E. (1980) Satellite vacuum ultraviolet airglow and auroral observations, J. Geophys. Res. 85:2201.

23. Gentieu, E.P., Feldman, P.D., and Meier, R.R. (1979) Spectroscopy of the extreme ultraviolet davglow at 6.5 A resolution: Atomic and ionic emissions between 530 and 1240 A, Geophys. Res. Lett. 6:325.

24. Tinsley, B.A., and Bittencourt, J.A. (1975) Determination of F region height and peak electron density at night using airglow emissions from atomic oxygen, J. Geophys. Res., 80:2333.

25. Chandra, S., Reed, E.I., Meier, R.R., Opal, C.B., and Hicks, G.T. (1975) Remote sensing of the ionospheric F layer by use of OI 6300 A and OI 1356 A observations, J. Geophys. Res. 80:2327.

26. Bauer, S.J. (1973) Physics of Planetary Ionospheres, Springer, New York, p. 183.

27. Schunk, R.W., and Nagy, A.F. (1980) Ionospheres of the terrestrial planets, Rev. Geophys. Space Phys. 18:813.

28. Evans, J.V. (1975) A review of F region dynamics, Rev. Geophys. Space Phys. 13:887.

29. Baumgardner, J., and Mendillo, M. (1983) Airglow imaging of ionospheric structures near the geomagnetic equator (Abstract), EOS, Trans. Am. Geophys. Union 64:275.

30. Sahai, Y., Bittencourt, J.A., Teixeira, N.R., and Takahashi, H. (1981) Simultaneous observations of OI 7774 A and OI 6300 A emissions and correlative study with ionospheric parameters, J. Geophys. Res. 86:813.

31. Strickland, D.J., Jasperse, J.R., and Whalen, J.A. (1983) Dependence of auroral FUV emissions on the incident electron spectrum and neutral atmosphere, J. Geophys. Res. 88:8051.

32. Hardy, D.A., Gussenhoven, M.S., and Huber, A. (1979) The Precipitating Electron Detectors (SSJ/3) for the Block 5D/Flights 2-5 DMSP Satellites: Calibration and Data Presentation, AFGL-TR-79-0210, AD A083136.

33. Weber, E.J., Buchau, J., Moore, J.G., Sharber, J.R., Livingston, R.C., Winningham, J.D., and Reinisch, B.W. (1983) F-layer ionization patches in the polar cap, J. Geophys. Res. (in press).

34. Paresce, F., Chakrabarti, S., Bowyer, S., and Kimble, R. (1983) The extreme ultraviolet spectrum of dayside and nightside aurora: 800-1400 A, J. Geophys. Res. 88:4905.

35. Strickland, D.J., Book, D.L., Coffey, T.P., and Fedder, J.A. (1976) Transport equation techniques for the deposition of auroral electrons, J. Geophys. Res. 81:2755.

36. Spiger, R.J., and Anderson, H.R. (1975) Electron currents associated with an auroral band, J. Geophys. Res. 80:2161.

37. Craven, J.D., and Frank, L.A. (1976) Electron angular distribution above the dayside auroral oval, J. Geophys. Res. 81:1695.

38. Rees, M.H., Stewart, A.I., Sharp, W.E., Hays, P.B., Hoffman, R.A., Brace, L.G., Doering, J.P., and Peterson, W.K. (1977) Coordinated rocket and satellite measurements of an auroral event, 1. Satellite observations and analysis, J. Geophys. Res. 82:2250.

39. Sharp, W.E., Rees, M.H., and Stewart, A.I. (1979) Coordinated rocket and satellite measurements of an auroral event, 2. The rocket observations and analysis, J. Geophys. Res. 84:1977.

40. Strickland, D.J. (1981) Electron Transport, Chemistry and Optical Emissions in the Auroral E-layer, AFGL-TR-81-0042, AD A102345.

41. Robinson, R.M., and Vondrak, R.R. (1981) Chatanika, Radar Measurements During the Auroral E Program, AFGL-TR-81-0238, AD A107117.

42. Swider, W., and Narcisi, R.J. (1981) Problems with the $N_2 + O \rightarrow NO^+ + N$ reaction in aurora, Geophys. Res. Lett. 8:1239.

43. Van Tassel, R.A. (1982) Rocket-borne Measurements of Optical Emission from the Auroral E-Layer, AFGL-TR-82-0354, AD A127517.

44. Whalen, J.A. (1981) General characteristics of the auroral ionosphere, in Physics of Space Plasmas, SPI Conf. Proc. Reprint Ser., 4, Ed. by T.S. Chang, B. Coppi, and J.R. Jasperse, Scientific Publishers, Cambridge, Massachusetts.

45. Hanson, W.B., and Carlson, H.C. (1977) The Ionosphere, from the Upper Atmosphere and Magnetosphere, National Academy of Sciences, Washington, D.C.

B1. Eather, R.H., and Reasoner, D.L. (1969) Spectrophotometry of faint light sources with a tilting-filter photometer, Appl. Optics, 8:227.

B2. Rohrbaugh, R.P., Tinsley, B.A., Rassoul, H. Sahai, Y., Teixeira, N.R., Tull, R.G., Doss, D.R., Cochran, A.L., Cochran, W.D., and Barker, E.S. (1983) Observations of optical emissions from precipitation of energetic neutral atoms and ions from the ring current, J. Geophys. Res. 88:6317.

B3. Torr, D.G., Torr, M.R., Hoffman, R.A., and Walker, J.C.G. (1976) Global characteristics of 0.2 to 26 keV charged particles at F region altitudes, Geophys. Res. Lett. 3:305.

Appendix A

Technique for Relating Intensities to the Electron Density Profile

Chandra et al[25] and Tinsley and Bittencourt[24] independently suggested a method for determining nighttime F region electron densities using airglow emissions based on three points: (1) at middle latitudes, the altitude profile of the electron density at night can be modeled with a modified Chapman function. (2) For a modified Chapman function, emissions resulting from radiative recombination depend only on the peak electron density (and very weakly on temperature). (3) Emissions resulting from dissociative recombination depend on the peak density, the altitude of the peak, and the exospheric temperature. These three statements must be qualified to some extent, but their general validity makes this method practical.

The first point allows the ionosphere to be characterized by two parameters: the peak electron density, $N_m F_2$, and the altitude of the peak, $h_m F_2$. In practice any reasonable approximation to the electron distribution would do as long as it is determined by two parameters. (The modified Chapman function actually depends on a third parameter, the exospheric plasma temperature. The sensitivity of the method to this parameter will be discussed below.)

A1. RADIATIVE RECOMBINATION FEATURES

Because O^+ is the dominant ion in the F region, the radiative recombination rate is proportional to the square of the ambient electron density and is independent of atmospheric composition. The volume emission rate of an optically thin feature resulting from this recombination also depends only on electron density. The column emission rate of such a feature is primarily due to emission from the vicinity of the electron peak. Consequently, the column emission is relatively insensitive to the exact shape of the electron density distribution, that is, to the exospheric temperature. Since no neutral species is involved, the column rate is independent of the altitude of the peak and provides a clean determination of peak electron density.

A list of atomic oxygen emission features produced by radiative recombination along with their partial recombination coefficients is given in Table A1. Because the atmosphere is transparent to wavelengths longer than 4000 A, reflection and scattering from the ground and from clouds and aerosols can be a problem. Between 3000 A and 4000 A Rayleigh scattering from lower levels of the atmosphere is another problem. For satellite observations, emission features at wavelengths shorter than 3000 A are to be preferred. Of these, the strongest are 1356 A and 1304 A. The line at 1304 A is optically thick but it may be used as long as the satellite is located several scale heights above the F peak. Both 1304 A and 1356 A have contributions from ion-ion recombination ($O^+ + O^- \rightarrow O + O + h\nu$). This introduces a dependence on the atomic oxygen density. The 911 A continuum and the line at 1027 A are free of this complication, but the intensity of 1027 A is certain to be unacceptably small. Although the normal midlatitude ionosphere is usually free of emission features near 1304 A and 1356 A, Huffman et al[22] have observed N_2 LBH band emission with intensities up to 1 kR at northern midlatitudes. The cause of the emission and its frequency of occurrence have not yet been determined. Whenever the LBH bands are present they will preclude the use of 1356 A and probably 1304 A as monitors of $N_m F_2$. This issue requires more study (see also Appendix B).

A2. DISSOCIATIVE RECOMBINATION FEATURES

Besides direct recombination, O^+ can undergo charge exchange with O_2. The resulting molecular ion dissociatively recombines leaving one or more oxygen atoms in an excited state. Each excited atom can be quenched by N_2, or it can emit a photon. Because the production rate of excited atoms is proportional to the product of the O_2 density and the O^+ density, the column emission rate of any of

Table A1. Parameters for Atomic Oxygen Emission Features

Radiative Recombination Features		
Wavelength (A)	Partial Rate Coefficients (cm^3 sec^{-1})	
	Radiative	Ion-ion
911 continuum	3.8×10^{-13}	-----
1027	9.0×10^{-14}	-----
1304	4.0×10^{-13}	6.9×10^{-8}
1356	8.1×10^{-13}	8.1×10^{-8}
4368	8.0×10^{-15}	-----
7774	5.8×10^{-13}	6.2×10^{-8}
8446	2.6×10^{-13}	6.9×10^{-8}

Dissociative Recombination Features	
Wavelength (A)	Transition Rates (sec^{-1})
2972	4.5×10^{-2}
5577	1.06
6300	5.15×10^{-3}
6364	1.66×10^{-3}

Sources:

Tinsley, B.A., and Bittencourt, J.A. (1975) Determinations of F region height and peak electron density at night using airglow emissions from atomic oxygen, J. Geophys. Res. 80:2333.

Tinsley, B.A., Christensen, A.B., Bittencourt, J.A., Gouveia, H., Angreji, P.D., and Takahashi, H. (1973) Excitation of oxygen permitted line emissions in the tropical nightglow, J. Geophys. Res. 78:1174.

Olsen, R.E., Peterson, J.R., and Mosely, J. (1971) Oxygen ion-ion neutralization reaction as related to tropical nightglow, J. Geophys. Res. 26:2516.

Kernahan, J.H., and Pang, H.L. (1975) Experimental determination of absolute A coefficients for "forbidden" atomic oxygen lines, Can. J. Phys., 53:455.

the resulting emission features is a strong function of h_mF_2. By using one of the radiative recombination features to determine N_mF_2, a dissociative recombination feature can be used to determine h_mF_2. Unlike the radiative recombination features, the dissociative recombination features are strong functions of the exospheric temperature. This is due to their dependence on the density of O_2 and N_2.

Consequently, a model atmosphere must be specified before the determination of h_mF_2 can be made. The principle dissociative recombination lines are at 2972 A, 5577 A, 6300 A, and 6364 A. Both 2972 A and 5577 A are also produced at lower heights as a result of non-ionospheric processes. Since this non-ionospheric contribution to the column intensities cannot be separated, 2972 A and 5577 A are unsuitable as ionospheric monitors. Both 6300 A and 6364 A are produced by decay of $O(^1D)$ and are strongly quenched at E region altitudes. However, the intensity of 6300 A is approximately three times that of 6364 A making 6300 A the feature of choice.

A3. DIRECT AND INVERSE CODES

We have developed two computer codes based on the formulae given at the beginning of Section 4. One code ("direct code") calculates the column intensities of 1356 A and 6300 A from a given electron density distribution. The electron density may be specified in tabular form, or it may be obtained from the modified Chapman function by specifying N_mF_2 and h_mF_2. The other code ("inverse code") determines the values of N_mF_2 and h_mF_2 from given values for the column intensities of the 1356 A and 6300 A features. It uses a modified Chapman function for the shape of the electron density profile. Both codes use the model atmosphere of Jacchia.[11] Table A2 lists the chemical reactions used in the two codes.

Table A2. Reaction Rates Used in Nighttime Codes

Reaction	Rate ($cm^3\ sec^{-1}$)
$O^+ + O_2 \rightarrow O_2^+ + O$	2.0×10^{-11} (300/T)
$O^+ + e \rightarrow O + O$	1.0×10^{-7} (700/T)
$O^+ + N_2 \rightarrow NO^+ + N$	1.0×10^{-12} (300/T)
$NO^+ + e \rightarrow N + O$	2.0×10^{-7} (700/T)
$O + e \rightarrow O^- + h\nu$	1.3×10^{-15}
$O^- + O^+ \rightarrow O^* + O$	1.5×10^{-7}
$O^- + O \rightarrow O_2 + e$	1.4×10^{-10}
$O(^1D) + N_2 \rightarrow O(^3P) + N_2$	7.0×10^{-11}

All rates were taken from Tinsley and Bittencourt (see Table A1).

Figures A1 through A3 show some of the output from a sample run of the direct code using $N_mF_2 = 5 \times 10^5$ cm^{-3}, $h_mF_2 = 350$ km, and an exospheric temperature of 1000 K. The electron density profile calculated from the modified Chapman function is shown in Figure A1. The volume emission rates for 6300 A and 1356 A are shown in Figure A2. The various production and loss terms in the chemistry of O(^{1}D) are shown in Figure A3. The resulting column emission rates are 4 Rayleighs (20% ion-ion recombination, 80% radiative recombination) for 1356 A and 45 Rayleighs for 6300 A.

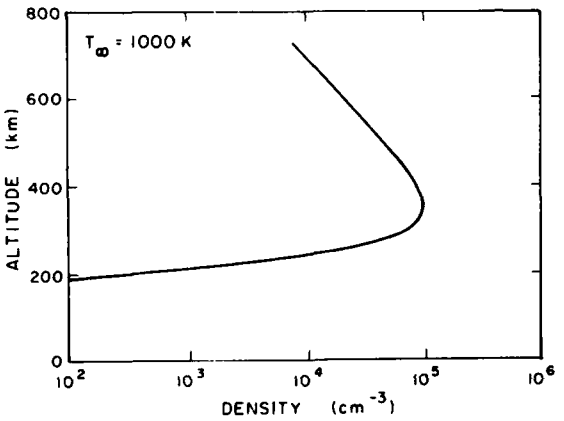

Figure A1. Altitude Profile of Electron Density Calculated From a Modified Chapman Function With $N_mF_2 = 5 \times 10^5$ cm^{-3} and $h_mF_2 = 350$ km

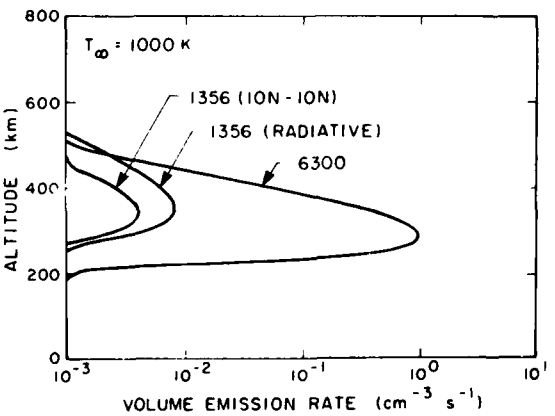

Figure A2. Volume Emission Rates for 6300 and 1356 S Calculated From the Electron Density Profile of Figure A1

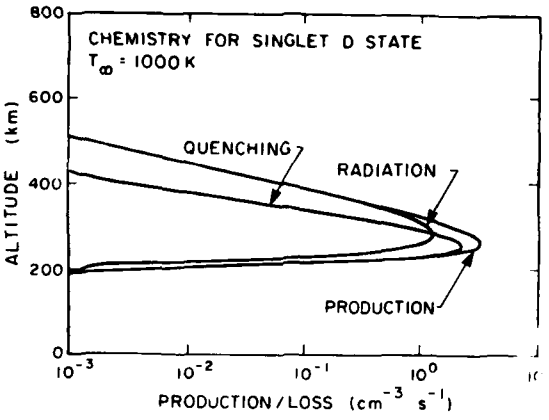

Figure A3. The Production and Loss Terms for O(^{1}D) Chemistry Calculated From the Electron Density Profile of Figure A1. Below 250 km, the dominant loss term is quenching by N_2, while radiation dominates above 350 km. This is the cause of the strong dependence of the 6300 A column intensity on h_mF_2

The two codes provide a useful tool for investigating nighttime emissions and their utility as ionospheric monitors. They can be used to test emission features other than 1356 A and 6300 A as well as predicting the emissions that will be produced for a given ionospheric scenario. They have been used in the experimental comparisons described in Section 4.2.

Appendix B

Factors Controlling Accuracy

B1. PROPOSED DETECTION SYSTEM

An optical system intended for use in remote sensing of the ionosphere must be capable of accurately measuring as little as 1 Rayleigh of the atomic oxygen line at 6300 A, 0.05 Rayleigh of the lines at 1356 A and 1304 A, and (if possible) 0.02 Rayleigh of the atomic oxygen continuum emission near 911 A. The 6300 A line falls at the red end of the visible spectrum, while the other features of interest fall in the far ultraviolet. Because of the different problems which are encountered in these very different spectral regions, there must be two systems: one for the visible and one for the ultraviolet.

The visible system should consist of a tilting filter photometer[B1] centered at 6300 A, with a bandwidth of 2.5 A, and the capability of scanning to about 6270 A. The last capability allows the background to be measured and subtracted from the total signal. A further advantage of the ability to scan in wavelengths, is that the wavelength bandpass can be calibrated in flight using the 6300 A line and the nearby OH line as precise wavelength standards. This permits the instrument system to compensate for temperature effects on the filter bandpass. Some means of in-flight calibration of instrument sensitivity should be provided. A standard source which could be moved in front of the photometer is one possibility. Observing

---

B1. Eather, R.H., and Reasoner, D.L. (1969) Spectrophotometry of faint light sources with a tilting-filter photometer, Appl. Optics, 8:227.

moonlight reflected from a surface of known albedo (for example, the cloudless ocean) is another.

The far ultraviolet system should consist of some combination of photometers and spectrometers. Since one or more spectrometers covering the extreme and vacuum ultraviolet spectral regions is necessary for monitoring the daytime ionosphere, the same system can also be used at night. However, it would be desirable to include one or more photometers for use when the nighttime emissions are at their weakest. Spectrometers provide greater wavelength resolution than photometers, but at the cost of reduced ability to detect weak emissions. The greater wavelength resolution is useful for separating the 1304 A and 1356 A features. It is also useful for detecting, and in some cases removing, background signals. Photometers can be designed with considerable light collecting power, and are especially useful at detecting very weak emissions. Unfortunately, the bandwidths available in the vacuum ultraviolet are greater than 100 A. This makes resolving the 1304 A and the 1356 A features very difficult, and subtracting a strong background next to impossible. A compromise between wavelength resolution and sensitivity is provided by a spectrometer such as the one used by Huffman et al.[22] Its bandpass could be increased to 25 A at which point it had an instrument response of 56 counts R^{-1} sec^{-1}. This is sufficient to observe even 0.05 R of 1356 A emission if the signal is counted for 30 sec or more. A typical UV photometer has an effective instrument response of 1220 counts R^{-1} sec^{-1} for the combined 1304 A and 1356 A features. This means that a counting time of 1.5 sec is sufficient. Thus, a photometer should be the main component of the far ultraviolet system with the daytime spectrometer as a supplementary system. The far ultraviolet system should also contain some means of in-flight calibration.

B2. FACTORS WHICH AFFECT THE ACCURACY OF THE DEDUCED IONOSPHERIC PARAMETERS

There are a number of factors which limit the accuracy of the ionospheric parameters inferred from atmospheric optical emissions. Some of these factors are related to instrument characteristics such as calibration and sensitivity. Others are related to extraneous sources of optical emissions such as reflection and scattering, particle precipitation, and low altitude (non-ionospheric) airglow. The remainder are related to inaccuracies in model representations of the ionosphere and the neutral atmosphere. These factors are not all unrelated, but some are more important than others.

B2.1 Instrumental Uncertainties

There are two main sources of instrumental uncertainty: calibration and sensitivity. Optical instruments are usually calibrated by determining the sensitivity of the instrument to a standard light source with known properties. Any uncertainty in the standard light source introduces uncertainty into the determination of instrumental sensitivity. Standard light sources are generally derived from photodiodes calibrated by the National Bureau of Standards. These photodiodes are used to calibrate the actual light sources which are used to calibrate the instrument. The photodiode calibration is characterized by the "probable error", a statistical estimate of the uncertainty of calibration. Each step in the process of transferring the calibration from the NBS photodiode to the instrument introduces additional uncertainty. Since the errors are uncorrelated, the probable error of the complete calibration process is the square root of the sum of the squares of the probable errors of each individual step. For example, if the original NBS calibration has a probable error of 8%, and if two additional steps with probable errors of 5% and 6% are required to calibrate the instrument, then the stated value of the sensitivity has a probable error of 11%.

Even if the sensitivity of the instrument were known exactly, an actual measurement of the intensity of an optical emission features would still have an uncertainty caused by the statistical nature of the measurement. Most optical instruments are essentially photon counters. The sensitivity of the instrument is measured in counts per photon. The probable error of counting photons is inversely proportional to the square root of the number of counts. If the instrument has registered 100 counts, then the probable error is about 10%. If it has only registered 10 counts, the probable error is 32%. If the observed light source is very weak, the instrument must accumulate counts until the probable error is within acceptable limits. For example, the proposed spectrometer for observing the 1356 A line has a response of 56 counts $R^{-1}s^{-1}$. If the intensity of the 1356 A is 0.05 R and the instrument counts for 30 sec, then the total number of counts is 83 and the probable error is 11%. The required accumulation time can be decreased only by increasing the sensitivity of the instrument.

Two other sources of error are the uncertainties in the determination of the collection aperture and field of view (solid angle) of the instrument. These measurements have probable errors of only 2 or 3% and make a negligible contribution to the overall measurement uncertainty. The counting rate of the instrument when no radiation is present, the dark count rate, is usually negligible in the laboratory (less than 1 count per second). In space, energetic particles produce dark count rates from a few counts per second up to 20 or 30 counts per second, depending on instrument design. These high dark counts occur mainly in the polar

regions, and dark count rates of a few per second are the norm. The effect of dark counts on the measurement uncertainty is discussed in the next section.

B2.2 Background Uncertainties

The actual counting rate of an optical instrument is the sum of the dark count rate, the counting rate produced by the emission feature of interest, and the counting rate of other features which happen to lie within the wavelength resolution of the instrument. When the instrument is located above the emission source region and is looking down, some of the incident light is due to scattering and reflection by the lower atmosphere and surface. In order to relate the measured intensity of an emission feature to the ionosphere, the fraction of reflected and scattered light must be known. For ultraviolet emission features, this fraction is vanishingly small. For visible features, the fraction can approach 50%. Thus, in order to determine the intensity of any emission feature, the dark count rate, the various sources of background emission, and the effective albedo of the earth and lower atmosphere must also be measured.

The dark count rate is easily determined by closing a shutter to block out external light. The background can be determined by scanning in wavelength so that the intensity of the adjacent continuum and discrete features can be measured. The continuum background is due to reflected light from astronomical sources: moonlight, starlight, and zodiacal light. Since the intensities of these light sources are well known, the measured value of the reflected intensities is a measure of the effective albedo. The measured dark and background counting rates must be subtracted from the nominal counting rate. This corrected counting rate must then be divided by the effective albedo plus one. The result is proportional to the apparent column emission rate of the feature in question. The conversion factor is determined by the sensitivity, aperture, and field of view of the instrument. Each step in this data reduction process adds to the estimate of the probable error of the measured intensity. Nevertheless, it is usually possible to keep the total uncertainty to 20% or less.

There are several circumstances under which the optical sensing method proposed above will fail. During magnetic storms, energetic oxygen atoms and ions are precipitated at midlatitudes from the ring current.[B2] These atoms and ions stimulate the emission of light by the ambient atomic oxygen. The resulting emissions obscure the 6300 A, 1356 A, and 1304 A emissions from the ambient

---

B2. Rohrbaugh, R. P., Tinsley, B. A., Rassoul, H., Sahai, Y., Teixeira, N. R., Tull, R. G., Doss, D. R., Cochran, A. L., Cochran, W. D., and Barker, E. S. (1983) Observations of optical emissions from precipitation of energetic neutral atoms and ions from the ring current, J. Geophys. Res. 88:6317.

ionosphere. They also produce a small amount of ionization in the E region. There are also occasions when energetic electrons and photons precipitate at mid-latitudes[B3] producing the same problem. As long as the E region ionization density remains small compared to F region densities, the OI 911 continuum radiation can give $N_m F_2$ (and thus TEC) even though the altitude of the F peak cannot be determined.

In addition to the two types of precipation events described above, N_2 LBH band emission is seen at midlatitudes.[22] The cause of this emission, which is a maximum in northern summer is unknown.[5] When it is present it obscures both OI 1304 A and 1356 A emissions, but does not effect either the 911 continuum or the OI 6300 A line. Thus the method described above will still produce the desired information, although the relative weakness of the 911 continuum will reduce the overall sensitivity of the method.

B2.3 Model Uncertainties

Once the intensities of two airglow features (usually the atomic oxygen features at 1356 A and 6300 A) have been determined, they may be used to determine $N_m F_2$ and $h_m F_2$ according to the techniques described in Appendix A. The probable errors associated with the two intensities translate into probable errors associated with the two ionospheric parameters. Because $N_m F_2$ is proportional to the square root of the 1356 A intensity, its probable error is half the probable error of the intensity. $h_m F_2$ is proportional to the ratio of the density to the 6300 A intensity. Most of the probable error associated with $h_m F_2$ is due to the probable error of the 6300 A intensity, but the $h_m F_2$ error scales as the log of the error of the 6300 A intensity, and remains relatively modest.

The preceding analysis is based on the assumption that the relationship between the two intensities and the two ionospheric parameters is exact. In reality the relationship is approximate, and its accuracy depends on the accuracy with which the shape of the electron density profile can be modeled. Because most of the emission comes from the region near the density peak, it is that region that must be modeled most accurately. The shape of the peak is determined largely by the temperature of the neutral atmosphere. Even in the worst case (full moon) the ionospheric parameters can be determined to within 30% using current technology. This contrasts favorably with ab-initio values which can be in error by factors of up to 5-10 during transport events. The implications of the measurement requirements for spatial resolution and coverage are described in Appendix C.

B3. Torr, D.G., Torr, M.R., Hoffman, R.A., and Walker, J.C.G. (1976) Global characteristics of 0.2 to 26 keV charged particles at F region altitudes, Geophys. Res. Lett. 3:305.

Appendix C

Operational Considerations

Among the many factors which will influence the final design of the proposed nighttime detector system (Appendix B), there are three which determine the ultimate utility of the system. Two of these are spatial resolution and spatial coverage. The third is the need for real time processing.

C1. SPATIAL RESOLUTION

The spatial resolution of the instrument is determined by two factors: the size of the field of view and the time required to make a measurement. (The latter is due to the motion of the spacecraft along its orbit.) A photometer with a circular field of view of 0.01 steradians, looking straight down from an altitude of 800 km, views a circle of diameter 50 km at the altitude of maximum electron density (about 350 km). This corresponds to less than half a degree of latitude. The center of the viewing area moves at 3.6° per minute (about 7 km/sec at an altitude of 350 km). The amount of time required to make a measurement depends on the intensities of the emission features and background and the instrument response. When the visible background is brightest (at full moon), the visible system may require as long as 1 min to make a measurement. This means that a measurement is made every 3.6° of latitude. When the background is low and both the ultraviolet and visible emission features are bright, it may be possible to make measurements

10 times per second. In this case the resolution is limited by the field of view because the spacecraft hardly moves during each measurement.

C2. SPATIAL COVERAGE

A satellite at an altitude of 800 km has a period of 100 minutes. During the time it takes the satellite to complete one orbit, the earth rotates about 25° in longitude. Consequently, a polar orbiting detection system views north-south swaths separated by 25° longitude. Practical considerations limit the field of view of any optical system so that the swath is at most a degree or two side. In order to monitor ionospheric conditions between these swaths, the system must be capable of scanning from side to side. For low background conditions, the system can obtain very complete longitudinal coverage even while maintaining high latitudinal resolution. When the background is high, it will be necessary to limit side to side scanning, and to eliminate it entirely in the worst cases.

C3. REAL TIME PROCESSING

On board real time processing will be essential to the operation of the nighttime detection system. In the first place, the system must be able to automatically select measurement time, scanning mode, and other instrument parameters to suite ionospheric conditions. In the second place, it will be very desirable for the system to convert the observed counting rates into ionospheric parameters on board. Given the current microprocesser technology, neither of these tasks should prove overly difficult. The first is routinely accomplished in modern satellite borne instruments. The second will require somewhat more effort.

The conversion of counting rates to ionospheric parameters proceeds in two major steps as described in Appendix A. First the background must be subtracted and the net counting rate converted to intensity. For the visible system, the effective reflectivity must also be determined so that the reflected light may be subtracted from the total. When the moon contributes to the background, the reflectivity must be corrected to take into account the fact that moonlight comes from a small source while airglow is a diffuse source. Data on the behavior of reflectivity for various surfaces (snow, vegetation, clouds, oceans) will have to be gathered, sorted, and put into a form (formulae, tables, and so on) which the onboard computer can use to make the correction.

The second major step is to convert the ultraviolet and visible intensities to ionospheric parameters. The onboard computer must have an accurate but fast algorithm for estimating neutral temperatures. The actual inversion will probably be based on iterated table look-up rather than the computer code described in Appendix A. Whatever algorithms are used, they must be fast enough so that spatial resolution and coverage are not compromised. This does not appear to be a major problem.

END

FILMED

4-85

DTIC